Irradiation-assisted stress corrosion cracking susceptibility and mechanical properties related to irradiation-induced microstructures of 304L austenitic stainless steel

Elie Paccou, Benoit Tanguy, Marc Legros

Irradiation-assisted stress corrosion cracking susceptibility and mechanical properties related to irradiation-induced microstructures of 304L austenitic stainless steel.

Elie Paccou [a,b], Benoît Tanguy [a], Marc Legros [b]

[a] CEA Saclay, Université Paris-Saclay, DEN, Service d'Etudes des Matériaux Irradiés, 91191 Gif-Sur-Yvette, France

[b] CEMES-CNRS, 29 rue J. Marvig, 31055 Toulouse, France

I. Abstract

304L SSs are used for structural components of Light Water Reactor (LWR) nuclear power plants and have been shown to face Irradiation Assisted Stress Corrosion Cracking (IASCC). This degradation phenomenon has been of great concern regarding structural integrity of reactors for lifetime extension of LWRs but is still not completely understood. This study evaluates the evolution of mechanical properties (hardening) and susceptibility to stress corrosion cracking regarding different radiation induced microstructures. These microstructures were chosen to explore representative conditions encountered in Pressure Water Reactor (PWRs) conditions but also the effect of various populations of cavities as extreme case of those reported at higher flux and temperature. Irradiation microstructures are produced by heavy ions irradiation under two different temperatures (450°C and 600°C) and with or without helium implantation. The evolution of microstructure, hardness and cracking susceptibility are characterized after irradiation. Calculations based on defects population are found to be in agreement with hardening measurement for irradiations with no helium implantation only. Cracking susceptibilities are characterized after slow strain rate tests performed at 4% plastic strain under PWR environment. Cracking susceptibility changes for different irradiations and quantitative assessment of the effect of irradiation microstructure on IASCC phenomenon is discussed.

II. Introduction

Structural materials used for fission reactor cores [1] or for ITER fusion reactor [2] are submitted to high energy neutron irradiation and high irradiation dose, leading to evolutions of mechanical properties related to irradiation defects creation in the microstructure. 300 series austenitic SSs (SS) are used for Light Water Reactors (LWR) core internals. Mechanical properties of these materials and their evolution with irradiation are required for design purposes, but also for ageing management, as several studies have shown a strong evolution of these properties (e.g. hardening increase, loss of ductility, fracture toughness decrease…) with irradiation. Better understanding of this degradation environment is clearly identified as a key-point issue for the maintenance costs diminution and potentially for the life extension of LWRs. Reviews of the degradation of austenitic SS mechanical properties with irradiation under LWR conditions can be found in Refs. [3–5]. Their evolution appears

to be strongly linked to the irradiation-induced microstructural features, as dislocation loops, precipitates, voids, bubbles formation or local chemical variations as radiation-induced segregation (RIS) although a clear relation relating mechanical properties and microstructure evolutions is not always clearly established. Amongst degradation phenomenon in LWRs, IASCC (Irradiation Assisted Stress Corrosion Cracking) has been shown to result from the synergetic effect of intense neutron irradiation, stress and corrosive environment (see e.g. [6,7]). Structural components as e.g. baffle-to-former bolts in PWRs or core shroud in Boiling Water Reactor (BWRs) were shown to be affected by IASCC in service conditions. Intergranular cracking susceptibility of irradiated SS stressed in a corrosive environment has been confirmed by numerous laboratory studies based on out-of-flux experiments (see e.g. [8,9]). RIS, which is described by elemental enrichment and depletion at point defects sinks like Cr depletion and Ni enrichment at grain boundaries (GB), was early identified as a contributor in GB cracking by enhancement of intergranular oxidation leading to reduction of GB strength [10,11]. In PWR's conditions, RIS role as the controlling detrimental factor was however questioned. Post irradiation annealing revealed that intergranular cracking susceptibility is decreased based on dynamic straining tests (slow strain rate test, SSRT) without measurable changes of Cr and Ni content at GB [12]. Radiation induced hardening was also identified as one of the main detrimental factor of IG cracking susceptibility. Role of hardening was clearly established in the IG cracking of cold worked SS where cracking susceptibility is observed above a minimum level of hardness [13]. Recent study [14] of the IG cracking susceptibility of low dose irradiated commercial and advanced alloys for LWRs internals has confirmed a correlation between cracking and hardening. However, in this study the authors did not conclude the controlling role of hardening. Irradiation-induced defects such as Frank loops act as dislocation barriers and thus contribute to irradiation hardening. This is confirmed by several studies that correlate measured increase of hardening (either by hardness or yield stress) to density and mean diameter of these population of defects through Orowan equation or other mechanistic models as reported e.g. in [15,16]. Cavities are also considered as barriers to dislocation motion. High strength factors are generally reported for voids in either in Body Centered Cubic (BCC) or Face Centered Cubic (FCC) materials. Mean value of 1 are generally considered for austenitics [17,18], whereas mean value of 0.6 was recently reported for BCC Fe [19]. Small bubbles (primarily He-gas filled cavities in neutron irradiated austenitics) are considered as weak barriers [17]. Defect-size dependence of strength factor was determined [20]. It is based on different hardening models and experimentally characterized number density and diameter bubbles induced by He irradiation in 316L. Depending on the hardening model considered, strength factor was shown to increase with bubble size or to have a relatively constant value [20]. A saturated value of ~0.2-0.3 was determined for bubble diameter higher than 15 nm. A continuous relationship between strength factor and voids size and density number was proposed for austenitic alloys in [21]. Role of small helium bubble both in the matrix hardening and in the embrittlement of grain boundary has been emphasized in nickel-based alloy with high helium concentration (1.8at% or 18000 appm He) [22]. Embrittlement role of He was evidenced in austenitic SS, where brittle intergranular fracture was shown for He concentration higher than 2at% [23]. In this study, the matrix hardening due to small He bubbles was point out as a concurrent parameter which enhances the brittle IG fracture, whereas the spacing of GB He bubbles is also inferred to play a detrimental role. Edwards and al. [24] reported observation of a high density (~ 10^{23} m^{-3}) of small cavities from TEM investigations of a thimble tube irradiated in PWR conditions at doses between 33 and 70 dpa. Although the He concentration was estimated to be ~0.07 at.% at the higher dose (based on an average ratio of 10 appm He/dpa), small bubbles containing high level of He

and hydrogen were inferred to promote IG failure and to increase susceptibility to IGSCC. Considering the He production rate estimated in PWR conditions, it is however very unlikely that He alone would be a unique factor controlling the IGSCC. Recently Villacampa et al [25] showed that the implantation of He up to 1000 appm (beside 2.2 appm of dissolved hydrogen) on 316L SS leaded to GB bubbles nucleation but did not impact IASCC initiation. Effect of helium embrittlement combined with radiation damage has then to be completed for austenitic SS. Further experimental data are required regarding the concurrent roles of the intragranular cavities on hardening and on GB cavities in fracture behavior to understand the IG cracking of neutron-irradiated SS.

Besides their recognized contribution to hardening, Frank loops are also a governing parameter in the enhancement of plasticity localization observed in strained irradiated SS. During deformation, radiation-induced Frank interstitial loops that are intersected by slip bands become unfaulted, assisted by the stress field of piled-up dislocations in the bands and are subsequently mostly cleared out the deformation band, this led to what has been reported as dislocation channeling [26] or "defect-reduced channel band" [27] i.e. the slip dislocations tend to become channeled in the defect-free and severely localized or inhomogeneous deformation occurs. Localized deformation has been proposed in several recent studies [28–30] as the most prominent factor in intergranular cracking susceptibility of plastically strained irradiated austenitic SS. Interaction between voids and dislocation channels that may arise from growing density number of voids with increasing dose naturally arises when considering the IASCC susceptibility evolution of highly irradiated components. Contribution of irradiation-induced voids to flow localization was early questioned in [31] related to ductile fracture mechanism in irradiated austenitic SS. Small He bubbles were reported to remain in the channels band in a He-irradiated 316LN strained at 10% [27]. In this study, the authors conclude that the deformation mode in presence of 2at.% He was not changed although cross-slip was restricted at a lower displacement damage level by the presence of helium. This observation was later confirmed by Jiao and Was [18] who showed that voids (size ranging from ~2 to 5 nm) were still present and relatively unchanged on the channel while dislocation loops were completely annealed.

The research referred to above illustrates the potential contribution of irradiation defects, here Frank loops and voids, on the embrittlement of irradiated SS. It is important to further understand the contribution of voids- and damage- hardening and localization on the IG cracking susceptibility of irradiated austenitic SS.

Neutron irradiations need long time irradiation because of relatively low damage rates in experimental reactors. They require costly evaluations since biological protections are needed. Self-ion irradiation is efficient and practical to evaluate radiation defects impact on IASCC. Indeed, it is possible to produce high flux of ions and then obtain high fluence rapidly at small costs compared to neutron irradiation. Irradiation experiments using an ion accelerator allow one to prepare samples containing different types of microstructure thanks to the flexibility of the irradiation conditions.

In this study different defects (voids and Frank loops) populations using self-ion irradiations are produced in order to study the effect of these defects on hardening and IG cracking susceptibility. Helium effect on voids size and density was also studied. Based on TEM characterizations of the irradiation induced microstructure and nanohardness tests, correlation between measured and calculated hardening was evaluated. Moreover, cracking susceptibility was determined based on SSRT tests in PWR environment. Existence of a correlation between defects population, hardening and

intergranular cracking susceptibility was finally assessed. Experimental procedures are described in the first part of the paper. Results of the characterizations (microstructural, nanohardness, and slow strain rate tests in PWR environment) are then detailed in the second part. Finally, analysis and discussion of the main results regarding the link between irradiation-induced microstructure, mechanical properties and cracking susceptibility in PWRs conditions are presented in the last part of the paper.

III. Experiment

A. Material

The material used in this study is a commercial grade AISI 304L SS. The chemical composition is Fe-18.75Cr-8.55Ni-0.02Mo-0.45Si-1.65Mn-0.012C-0.01P-0.002S (wt%). The material was solution annealed at 1050°C for 30 min followed by quenching with helium. Austenite is then the main phase beside ferrite (content measured to less than 5%). The mean grain size was 21 µm. Conventional yield 0.2% stress and tensile strength of the virgin material were determined at 340°C at a mean strain rate of 5. 10^{-4} s^{-1} and is equal to 200 ±5 MPa and 451 ±5 MPa, respectively. Machining of tensile specimens and bars was done based on electro-discharge technique. Tensile test specimens (gauge section of 18mm, 2x2 mm² cross section) were used to conduct slow strain rate tests whereas bars (length 18 mm, 2x2 mm² cross section) were dedicated to microstructural characterization. All samples were mechanically polished with SiC paper down to 2400 grade followed by diamond paste polishing down to 1 µm to have a mirror-like surface. Samples were then vibratory polished with colloidal silica to remove surface hardened zone induced by mechanical polishing. In order to characterize the microstructure induced by irradiation, TEM samples were prepared using the lift-out technique with a focused ion beam (FIB) system with the following steps: at first, walls were designed to be 10 µm long, 5 µm deep and 1 µm thick approximatively on irradiated surface of bar samples. A micromanipulator system was used to extract the walls from the bar samples and to fix them on Cu grids for further thinning. A low current was used to thin the wall to thin a lamella down to ~100 nm thickness.

B. Ion irradiations

Four campaigns of irradiations were conducted at CEA Jannus-Saclay platform with the objective to obtain different microstructures. For each campaign, a set of tensile samples and bars was prepared. Irradiation experiments were conducted using a 10 MeV Fe^{5+} ion beam, leading to a damage layer with a penetration depth of about 2.5 µm. Ion beam was raster-scanned with a horizontal frequency of 517 Hz and vertical frequency of 64 Hz. To avoid carbon contamination, prior plasma cleansing and a cold trap during irradiation were used, as suggested by Was at al. [32].

Irradiation damage and implantation profile were estimated using the software SRIM-2008 under Kinchin-Pease approximation (fast calculation mode) with a displacement energy for all elements fixed at 40 eV. As recommended in [33], dpa K-P was used in this study. The damage will be cited as simply dpa from now onwards. Unlike proton, the damage profile for Fe irradiation shows a continuous evolution of the damage (dpa). Therefore, the damage considered in this study will correspond to the

damage at the surface. In addition, the irradiated zone in each sample was 10 mm x 2 mm so that all samples had both irradiated and unirradiated ("virgin") regions. This helped to have comparative studies in irradiated and unirradiated conditions and to eliminate variations, which could be induced by surface preparation. Irradiation temperature was considered as a first parameter to vary the population of irradiation induced defects (mainly Frank loops and cavities). Two temperatures were considered. The first temperature was chosen at 450°C based on previous studies [34,35] in order to emulate a Frank loops microstructure representative of the one observed in neutron irradiated SS under PWR conditions. The temperature shift between PWR conditions and ion irradiation is needed to accommodate the higher flux rate under ion irradiation [36]. Considering the large difference of flux rate between neutron and ion (~ 10^{-4} dpa/s for ion in comparison to 10^{-8} dpa/s for neutron), it is noted that an irradiation temperature of 450°C is a compromise between the temperature calculated for microstructure (370°C) and the one calculated for similar microchemistry (RIS) (550°C). The second temperature was chosen at 600°C with the objective to emphasize the population of cavities and to limit the Frank loop population. Four thermocouples in contact with samples were used to measure the temperature during the irradiation as shown in Fig. 1a). Differences between these thermocouples, variation of temperature during ion flux measurement and during each irradiation campaign lead to small deviation from target temperature (see Results).

The second parameter considered in this study is implantation of helium ions. Helium implantation is used to emulate transmutation[1] that occurs in neutron irradiated SS [36]. Helium implantation was done with 1 MeV He^+ ions. An energy degrader system composed of five aluminum foils with different thicknesses and one hole had been placed in front of He beam to obtain a more homogenous implantation profile. The profile and depth of implantation were determined based on SRIM simulations of 1 MeV ion beam going through Al foils and the hole with the following two steps. The first step was to assess the mean energy of He beam and the ratio of He ions reaching the sample after going through an Al foil with a given thickness. The second step was to assess the He implantation profiles in SS for each Al foil based on the mean ion energy and flux values determined in the first step. He implantation profiles for each Al foil are then mixed together to form the complete He implantation profile in the material. Foils of 2.4 µm, 2 µm, 1.6 µm, 1.2 µm and 0.8 µm result in an implantation in depth between 500 and 1800 nm where the He content is higher than ~100 appm. Calculated damage rate is $3.36x10^{-6}$ dpa.s^{-1} for Fe-He-450 and $2.5x10^{-5}$ dpa.s^{-1} for Fe-He-600 which is two orders lower than the iron irradiation. He content of 15-20 appm/dpa was chosen in order to be representative of those encountered in core components in LWRs conditions. It is noted that despite than an energy degrader system was used, helium implantation is not uniform along the whole irradiated layer (see

Fig. *3*c and 3d). Average helium concentration at surface were calculated over the first 500nm to be equal to 50 appm and 25 appm in Fe-He-600 and Fe-He-450, respectively.

Damage and implantation profiles are shown in Fig. 1b) where the Fe implantation profile is similar for irradiations with and without He implantation. It is noted that helium implantation also induces radiation damage; however, considering the amount of helium implanted, it has been evaluated that the damage will be increased by less than 2.5 % so that only damage induced by Fe implantation is reported

[1] Helium can be produced by (n,α) reaction on Ni, Fe, Ti and Cr atoms with high energy neutrons (>1 MeV) and also by the successive $^{58}Ni(n,\gamma)\ ^{59}Ni(n,\alpha)\ ^{56}Fe$ reactions with thermal neutron energies [9].

in the following. Thereafter, “Fe-450”, “Fe-600” refer to single Fe ions irradiations performed at 450°C ± 20 °C, 600°C ± 25 °C, “Fe-He-450”, and “Fe-He-600” to Fe irradiations with He implantations performed at 450°C and 600°C, respectively. It is noted that at 600°C, He and Fe implantations were done successively whereas co-implantation was done at 450°C. Co-implantation mode at 450°C was chosen for a better emulation of physical mechanisms leading to cavities formation observed in PWR’s irradiation conditions whereas co-implantation at 600°C was not required with the objective to vary the cavities population [37].

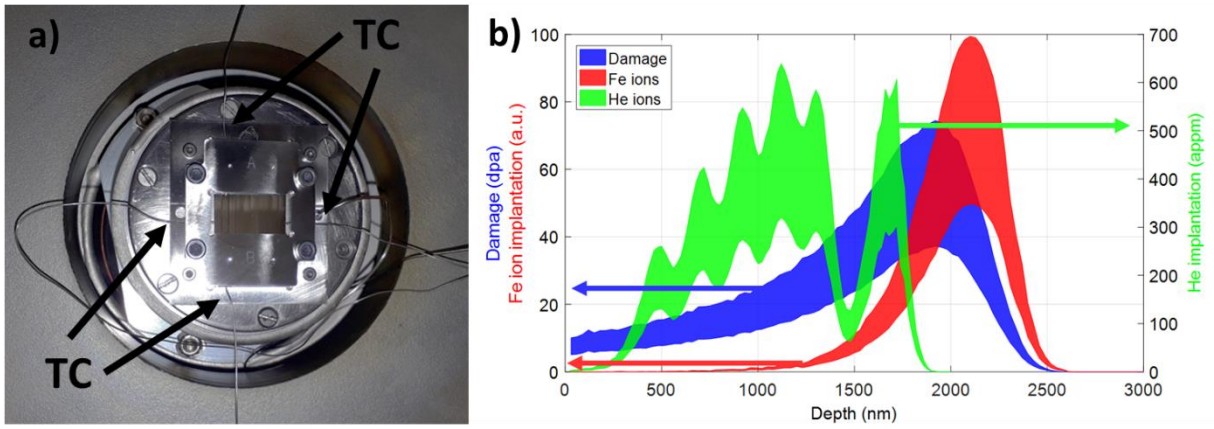

Fig. 1: a) Irradiation Set up showing the batch of samples in the irradiation chamber. Thermocouples (TC) are connected to the side of samples for temperature measurement. b) SRIM profile of Fe 10 MeV irradiation coupled with 1 MeV degraded He implantation in the case of Fe-He-450. The blue profile stands for damage profile in dpa, the red profile for Fe ions implantation in arbitrary units and the green profile for He ions implantation in appm by the use of an energy degrader. Width of the profile is associated with the uncertainty associated to each value.

Targeted doses were 20 dpa at the surface with a dose rate of ~4×10^{-4} dpa/s (calculated at the surface). Ion flux is measured periodically based on Faraday cups during irradiations. Fluence is calculated afterwards from the flux measured. However, post irradiation flux evaluations showed that the flux was overestimated. These evaluations were confirmed based on Rutherford Backscattering Spectrometry measurements of glassy carbon samples that were also included in the batch. This technique consists in bombarding the reference material (here glassy C) with 2.5 MeV H^+ ions that are backscattered and collected as a 160° spectrum. Quantification of this spectrum is based on the widely used "SIMNRA" software. Consequently, the doses obtained at the surface of the samples were lower. A mean value of 12±4 with a dose rate of ~2.2×10^{-4} dpa/s and ~2.4×10^{-4} dpa/s were evaluated at the surface for Fe-600 and Fe-He-600 respectively, whereas a mean value of 8±1 dpa with a dose rate of ~1.3×10^{-4} dpa/s was obtained for Fe-450. Fe-He-450 was carried out after the reevaluation of the dose rate so that a mean dose of 10±2.5 dpa with a dose rate of ~1.7×10^{-4} dpa/s was targeted in order to be close to the previous irradiations.

Table 1 resumes the irradiation conditions.

Table 1 : Irradiations details, dose, dose rate, fluence and implantation mode.

Irradiations	Dose at surface (dpa)	Dose rate at surface (dpa/s)	Fe fluence (ion/cm²)	He Implantation mode
Fe-600	12±4	$2.4\pm0.8 \times 10^{-4}$	$8.4\pm2.8 \times 10^{16}$	No He
Fe-He-600	12±4	$2.2\pm0.7 \times 10^{-4}$	$9.6\pm3.2 \times 10^{16}$	Pre implantation at 600°C
Fe-450	8±1	$1.3\pm0.2 \times 10^{-4}$	$9.6\pm3.2 \times 10^{16}$	No He
Fe-He-450	10±2.5	1.7×10^{-4}	$8.25\pm2.1 \times 10^{16}$	Co-implantation

C. Microstructure characterization

Microstructure were characterized after irradiations by the use of transmission electron microscopy (TEM) with a Tecnaï G² equipped with a LaB6 filament operating at 300kV. For every irradiation condition, cross section TEM samples are produced by the lift-out technique using a FEI Nanolab Dualbeam FIB. The same equipment is used for cross sectioning. Cross-section foils allow characterizing the total depth of the irradiated zone (~2.5 µm). Voids were detected by over-focus/under-focus technique, but their sizes were characterized using an under-focused beam. Frank loops were characterized by revealing one of the four families of these defects by the rel-rod technique using the diffraction conditions ([011] zone axis with g = ½ (3-11) diffusive line). Images acquired in different TEM lamellas were used to obtain a better statistic of each type of defects.

For density evaluations of the radiation-induced defects, TEM foils thickness is characterized by Electron Energy Loss Spectroscopy (EELS) zero loss method for each sample. After observation, defects are quantified using ImageJ software. Defects are manually selected and characterized by their size, number and position on the sample. Only one plane was observed and based on the homogenous distribution of Frank loops families [38] the number of Frank loops quantified was multiplied by four to evaluate Frank loops density. To have good statistics, quantification was done on more than 600 Frank loops for each irradiation condition.

D. Nanoindentation tests

In order to quantify the hardness evolution between irradiated and unirradiated microstructures, nanoindentation tests were performed. The same methodology was used than in [34,35] and will be only briefly recalled hereafter. A Nanotest platform III from Micro Materials Limited equipped with a Berkovich tip was used. The samples were indented normally onto the surface and a grid of 10 lines with 20 indents each were made corresponding to indent penetration depth ranging from 200 nm to 2 µm. The distance between the two consecutive indents and between two lines was 40 µm each to avoid interactions between plastic zones generated by each indent. Indentations were performed in depth-control mode. The duration of loading/unloading was fixed to 20s with the loading/unloading rate varying depending on the maximum load. A 20s hold time was used at the maximum load. The average of the 20 measured hardness values was calculated and considered for the corresponding indent penetration depth. Indentations are performed both in the irradiated and in the unirradiated areas of the sample to avoid any preparation effect in the determination of the hardness increases.

E. SSRT and IASCC susceptibility assessment

Cracking susceptibility assessment was made based on SSRT tests conducted in simulated nominal PWR primary water environment. The tests were carried out with a strain rate of 5 x 10^{-8} s^{-1} using tensile testing device CORMET C137. The same experimental device and test methodology than in [34,35] was used. The autoclave (5 liters capacity) was filled with primary water (25-35 cc/kg H_2 STP, 1000 ppm B, 2 ppm Li). The temperature of the system was increased to reach the test temperature of 340°C, and the pressure was maintained at 155 bars. PT (Pressure-Temperature) sensor located in the center of the autoclave was used to monitor pressure and temperature during the test. Prior to straining, environmental conditions were allowed to stabilize for few hours. Load was applied using a computer driven 30 kN load train. A displacement sensor LVDT (Linear Variable Displacement Transducer) located on the traction line of the autoclave measured the displacements. Load and displacement data were collected by a computerized data acquisition system and recorded every 10 seconds. Specimens were strained up to 4% plastic strain which correspond to a test duration of about 10 days.

F. IASCC susceptibility assessment

Following SSRT tests, cracks were characterized using scanning electron microscopy (SEM). Cracks existence, number of cracks, crack length and total crack length per unit area were used in this study as indicators of cracking susceptibility.

Sample surface is observed using a FEI NanoLab Dual Beam in SEM mode. An ICE detector to obtain a clear contrast between cracked and un-cracked grain boundaries collected backscattered electrons. Automated acquisition of SEM images was used in order to get large areas with high resolution. Images with a horizontal field of view (HFW) of 25 µm were collected in four different areas (~ 0.25 mm² each) of the irradiated zone to get more than 3000 images representing an observable total area of ~1.1 mm². These areas are located in the irradiated area of the specimen gauge length, with the first area being ~2 mm from the unirradiated/irradiated transition zone, the following areas being spaced every 2 mm so that the fourth area was located ~2 mm from the opposite irradiated/unirradiated transition zone. The same process is applied in the unirradiated zone of the samples.

Intergranular cracks were identified by their contrast in backscattering electron images: dark along the centre bordered by brighter edges. Cracks were manually identified and traced in ImageJ and these traces were measured using ImageJ software. The crack length of each crack was estimated by the measurement of the distance between the two ends of the crack considered. Crack is considered to exist when an opening of 4 pixels or more is seen on SEM images. In our case, 4 pixels corresponds to ~ 68 nm. For branched cracks, only the length which corresponds to the longest length has been considered. The assessment of a crack end has been defined at ±2 pixels, then the length of a crack is defined at ± 4 pixels, i.e. ± 68 nm. The uncertainty for density measurement was evaluated but is estimated to be small regarding statistical uncertainty.

The data on crack length thus obtained was converted into a crack length distribution profile from which the mean crack length was obtained. Statistical evaluation of the mean value of crack density and mean crack length were based on scanning two different areas of 1 mm^2 for each irradiation condition.

IV. Results

A. Microstructure

Microstructural characterization was done along the whole depth of the irradiated layer for each irradiation condition. Frank loops, voids and precipitates were investigated from TEM of cross-section samples. Fig. 2a) shows an example of Frank loops and voids observed in Fe-He-450 sample with Bright Field TEM imaging. Dark Field TEM image shown in Fig. 2b) allows isolating Frank loops from the microstructure. Frank loops or voids were not observed beyond the damage layer calculated with SRIM, i.e. beyond a depth of 2500 nm (see Fig. 1). It is also noted that based on imaging conditions exposed in the Fig. 4 of [38] (Beam condition to observe precipitates was B = [110] g= [220]. No spot was discovered between the transmitted (000) spot and the (220) spot), radiation induced precipitates such as γ' were not observed in the irradiated layer for the irradiation conditions studied. G-phase precipitates were not characterized. Densities and mean size of Frank loops and voids are given in Table 2. Values averaged over the whole depth and values at surface are reported in Table 2. Values at surface were calculated over the first 200 nm and were considered here to allow comparison with data reported in the literature which are mostly obtained from TEM foils located close to the irradiated surface.

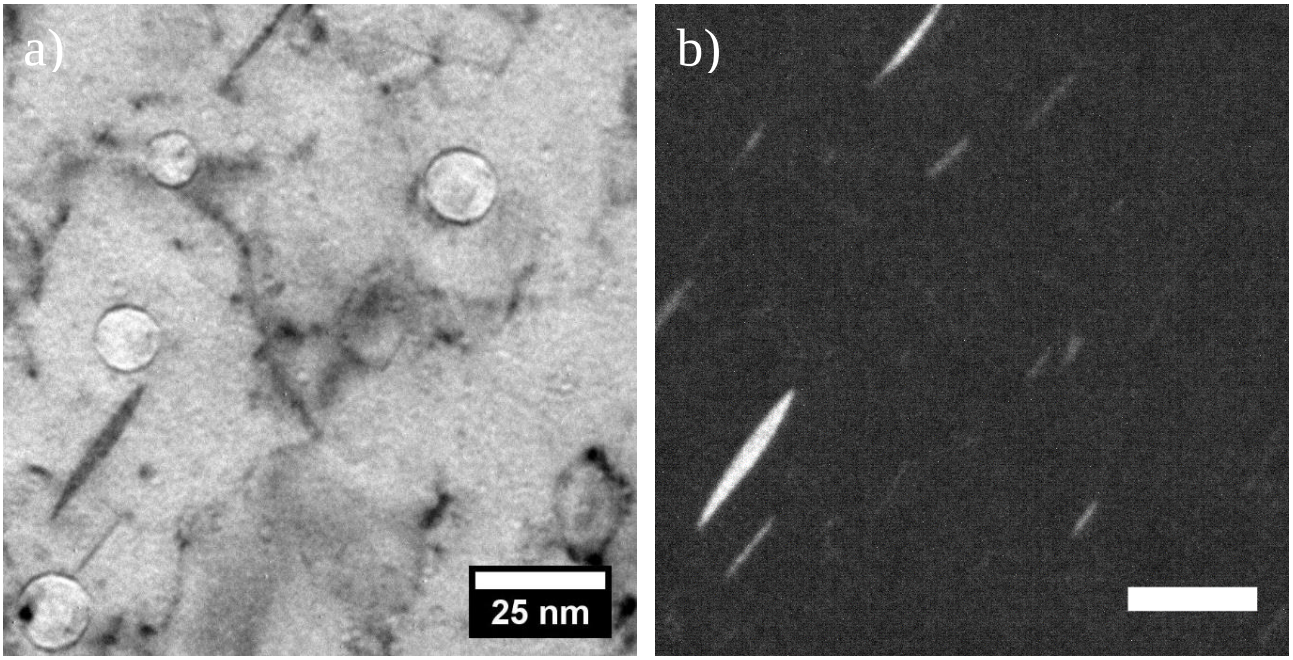

Fig. 2: a) Bright Field TEM image under-focus image showing Frank loops and voids and b) Dark Field TEM image of the same area showing Frank loops in Fe-He-450 condition.

Table 2 : Defects (voids and Frank loops) densities and size for the studied irradiation conditions (values at surfaces are the average value over the first 200 nm).

Irradiations	Dose at surface (dpa)	Voids						
		Density (m^{-3})		Density at surface (m^{-3})	Mean size (nm)		Size at surface (nm)	Volume occupied by voids (%)
Fe-600	12±4	$2.4\pm0.5\times10^{19}$		$1.15\pm0.3\times10^{19}$	110±1		78.5±1	2.7±0.1
Fe-He-600	12±4	$1.3\pm0.1\times10^{20}$ (small)	$4\pm0.4\times10^{18}$ (large)	$7.9\pm2\times10^{19}$	8.7±1 (small)	77±1 (large)	8.7±1	8.7±0.3
Fe-450	8±1	$4.2\pm0.8\times10^{20}$		$2.7\pm0.6\times10^{20}$	21.7±1		11.3±1	0.3±0.1
Fe-He-450	10±2.5	$2.7\pm0.8\times10^{22}$		$3.8\pm1\times10^{22}$	8±1		8.3±1	0.2±0.1

Irradiations	Dose at surface (dpa)	Frank loops			
		Density (m^{-3})	Density at surface (m^{-3})	Mean size (nm)	Size at surface (nm)
Fe-600	12±4	$< 10^{19}$	$< 10^{19}$	-	-
Fe-He-600	12±4	$< 10^{19}$	$< 10^{19}$	-	-
Fe-450	8±1	$1.1\pm0,2\times10^{22}$	$0.9\pm0,2\times10^{22}$	22.4±1	23.2±1
Fe-He-450	10±2.5	$1.1\pm0,3\times10^{22}$	$0.5\pm0,1\times10^{22}$	16.4±1	17.2±1

Cross section bright-field TEM images for the four irradiations conditions are shown on

Fig. 3. Profiles of damage, He and Fe implantation are superimposed on each image.

Fig. 3 shows that voids of various size were observed at both 450°C and 600°C and that the voids population is very sensitive to the irradiation conditions. The corresponding voids size distributions with corresponding density are given in Fig. 4.

These distributions confirm that the density of voids is markedly different depending on the irradiation condition. Large voids are obtained after irradiation at 600°C (Fig. 4c and d) whereas smaller voids are observed after irradiation at 450°C (see Fig. 4a and b). Comparison of Fig. 4a and b with Fig. 4c and d reveals a clear effect of helium implantation on the voids population. For both 450°C and 600°C, helium implantation leads to the presence of second population of smaller cavities with a high density resulting to a decrease of the mean void diameter (see Table 2). Small and large cavities distributions were clearly distinguished only for Fe-He-600. Cavities of Fe-He-450 and small cavities of Fe-He-600 both exhibit a spherical shape which means that they are in equilibrium with surface free energy of the material. The pressure P of these bubbles can then be calculated by the expression $P=2\gamma/r$. γ is the surface free energy which is 3.975 J/m² [41] and r the radius of the bubble. The pressure of bubbles is around 2 GPa for Fe-He-450 and 1.8 GPa for Fe-He-600. Considering the work of Villacampa on helium bubbles in austenitic stainless steel [20] the mean concentration of helium of ~40 He/bubble/nm^3 is deduced.

Voids distributions of size, frequency and volume fraction through the depth of irradiated layer are given on Fig. 5 (a, b, c) for Fe-450, Fig. 5 (d, e, f) for Fe-He-450, Fig. 5 (g, h, i) for Fe-600 and Fig. 5 (j, k, l) for Fe-He-600 samples. These distributions regarding depth clearly show that cavities are observed along the depth of the irradiated area up to ~2000 nm with a spatial distribution, which depends on irradiation conditions. No clear correlation between irradiation conditions and void spatial distribution can be evidenced from graphs on Fig. 5. For Fe-450 and Fe-He-450 the highest voids frequency is around 1800 nm whereas the highest frequency is closer to the surface at 600°C. As described earlier, a strong effect of helium implantation is observed on voids density and size. For 450°C irradiations, He co-implantation leads to a decrease of mean voids size (from 21.7 to 8 nm) and a marked increase of density (~x60). Mean porosity as calculated by the voids volume fraction varies from 0.2% (Fe-He-450) to 8.7% (Fe-He-600), the smaller porosity being obtained at 450°C (0.2% and

0.3% for Fe-He-450 and Fe-450, respectively) and larger porosity at 600°C (2.7% and 8.7% for Fe-600 and Fe-He-600, respectively). The mean volume fraction has been evaluated by taking into account the distribution of size and density over the whole damage area.

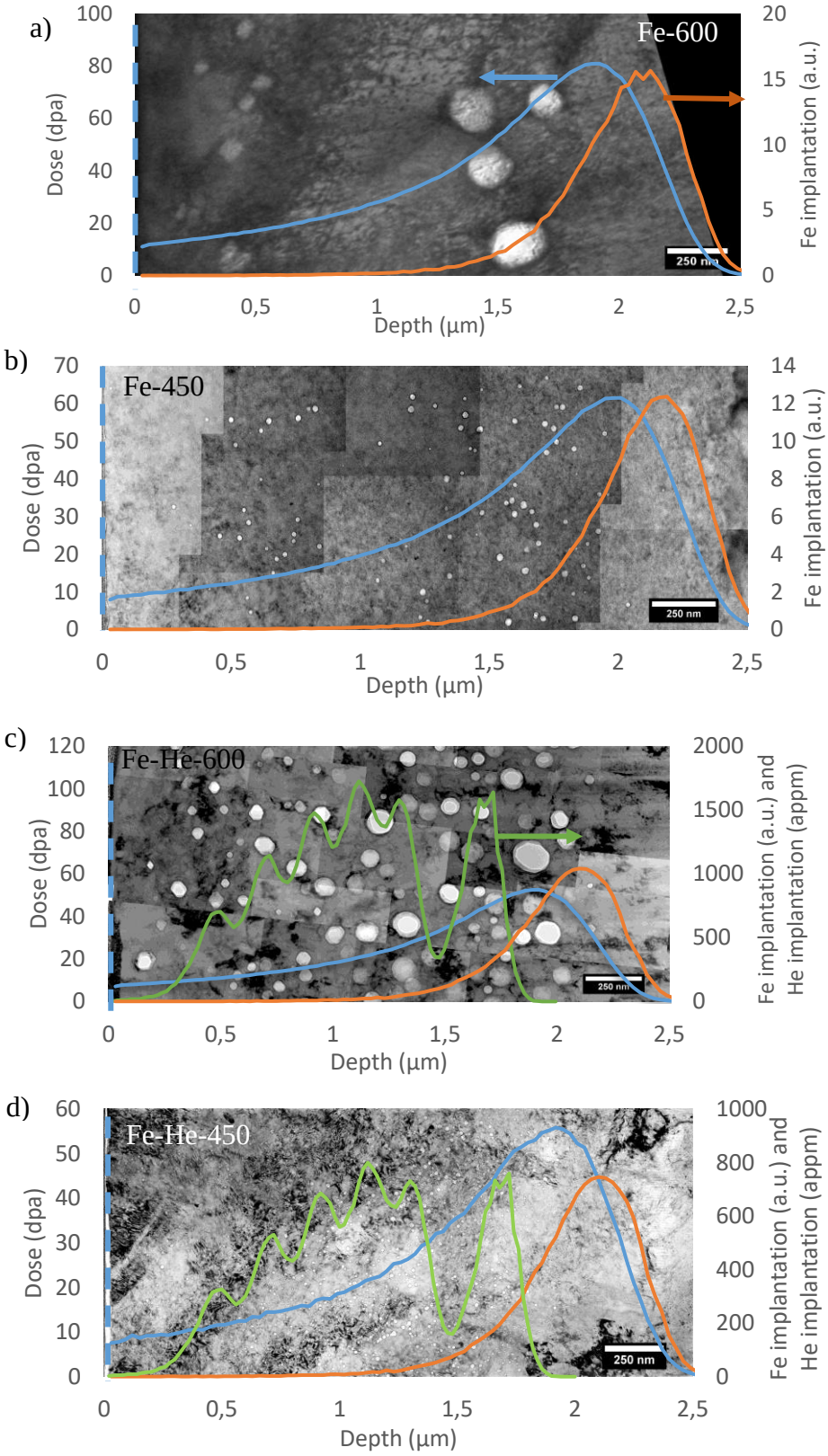

Fig. 3 : Voids observed in irradiated samples: a) Fe-600, b) Fe-450, c) Fe-He-600 and d) Fe-He-450 (dashed line on each graph represents the irradiated surface and solid color lines are explained in Fig. 1).

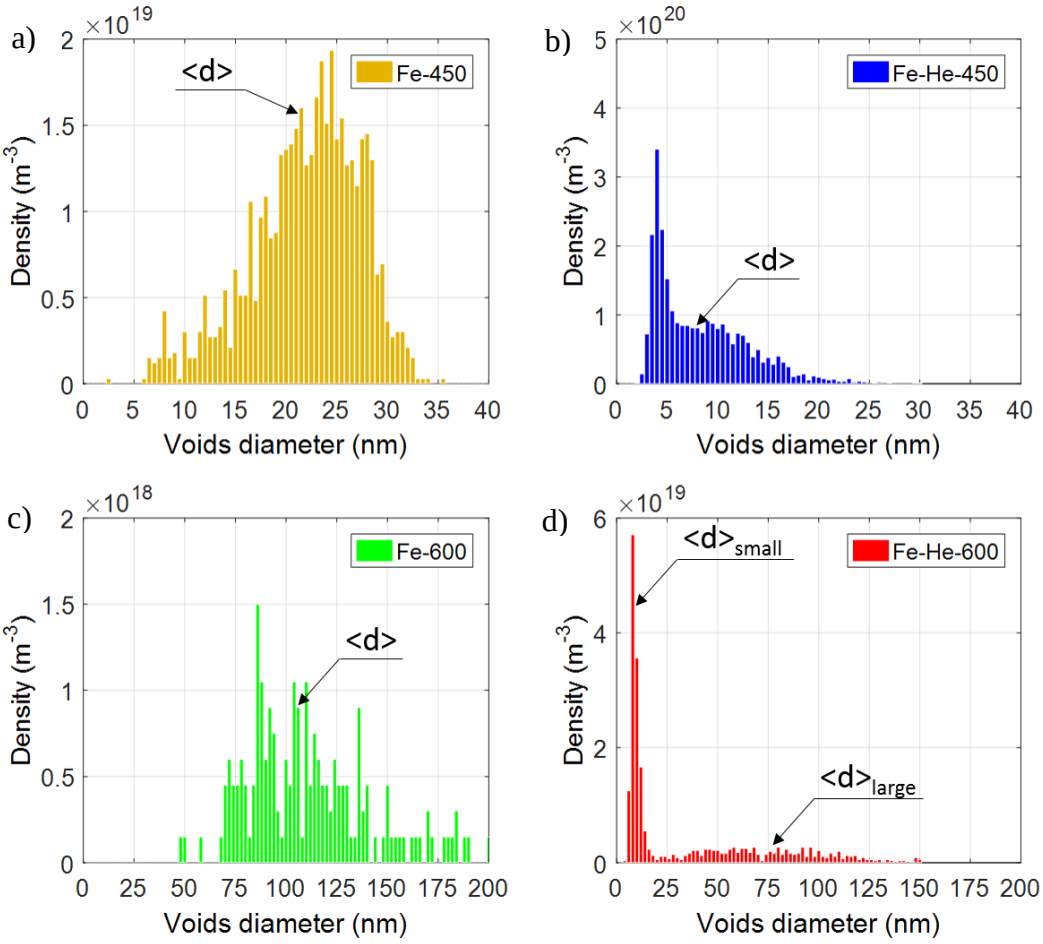

Fig. 4 : Void size distributions for (a) Fe-450, (b) Fe-He-450, (c) Fe-600 and (d) Fe-He-600. Step sizes of 0.5 nm are chosen for Fe-450 and Fe-He-450 irradiations while a step size of 2.5 nm is chosen for Fe-600 and Fe-He-600 irradiations. For each condition, the void average size is indicated by <d>. Values for <d> are given in Table 2.

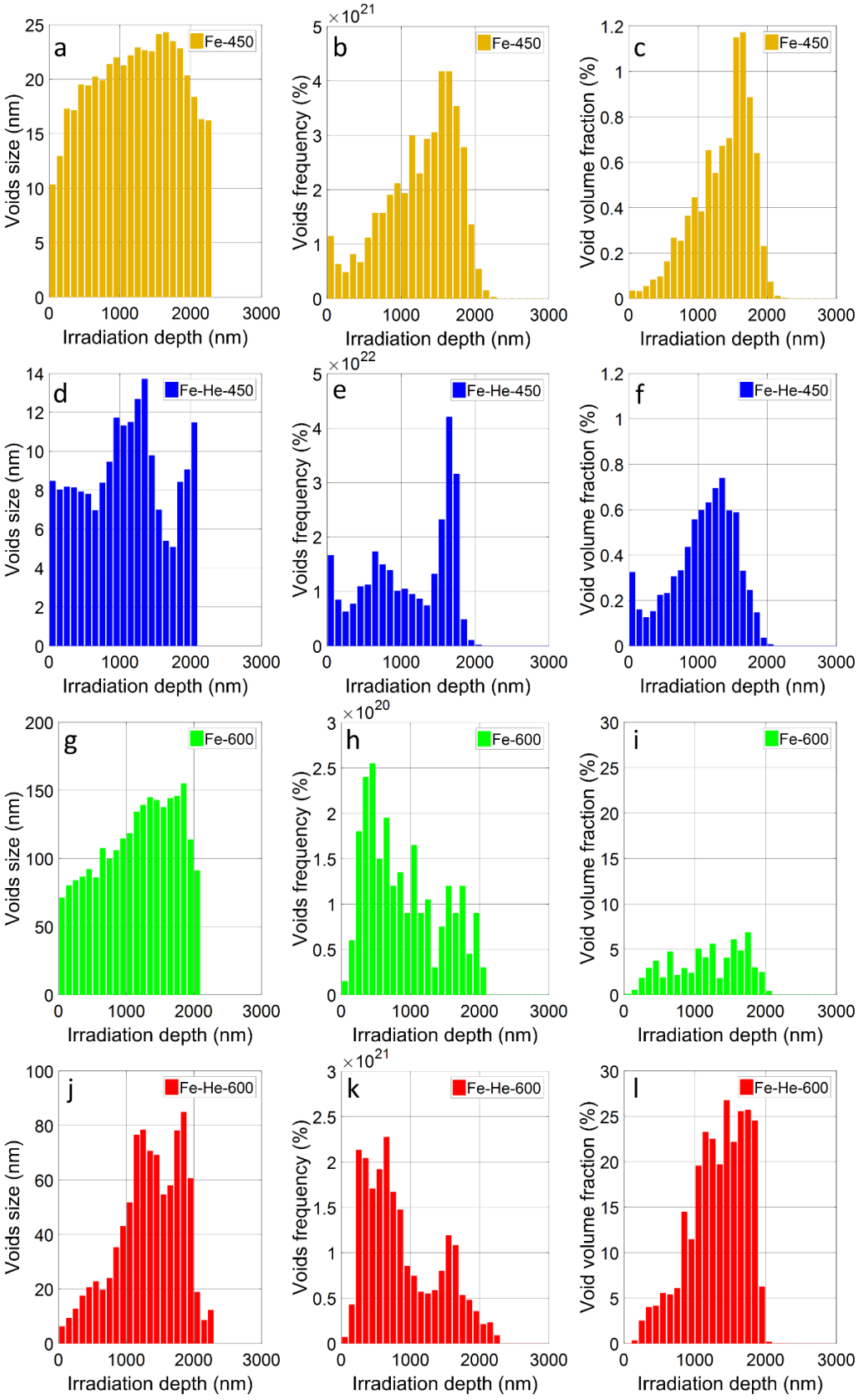

Fig. 5 : Void distributions for all irradiations. Size distributions (a,d,g,j), frequency distributions (b,e,h,k) and volume fraction distributions (c,f,I,l) are displayed for Fe-450 (a,b,c), Fe-He-450 (d,e,f), Fe-600 (g,h,i), and Fe-He-600 (j,k,l). A step of 100 nm is used for all distributions.

Intergranular nanocavities (IG cavities) were observed for Fe-He-450 and Fe-He-600 (see red arrows on Fig. 6) but not for Fe-600 and Fe-450. The observed cavities were located at high-angle grain boundaries (HAGB). Moreover the presence of these cavities appears to be closely related to the He content: they are observed where the He implantation is maximum whereas IG cavities were not observed at a depth of 1500 nm where He implantation has strongly decrease nor close to the surface where He is not implanted (depth <~500 nm). IG cavities size and mean spacing depends on the irradiation conditions: a mean size of 8.8 nm and 5.1 nm for Fe-He-600 and Fe-He-450, respectively with a mean spacing of 77 nm and 55 nm. The cavities on the grain boundaries are smaller than their counterparts in the alloy matrix for Fe-He-450 and correspond to the population of small cavities observed in the matrix for Fe-He-600.

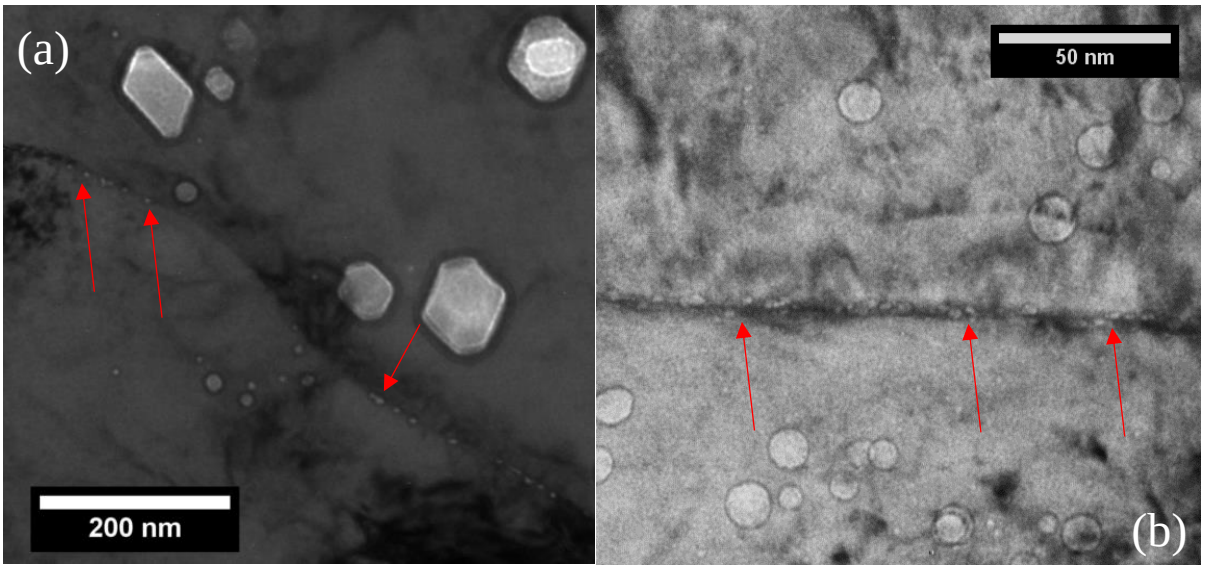

Fig. 6: Intergranular voids** (red arrows) **on Fe-He-600 (a) and Fe-He-450 samples (b).

Frank loops were observed with a high density after 450°C irradiations and barely observed after 600°C irradiation. The Frank loops size distributions and density distribution regarding irradiation depth for the two 450°C irradiations are given on Fig. 7. No effect of helium implantation is observed in mean Frank loop densities (~1.1×10^{22} m^{-3}) though distribution regarding depth are not exactly the same as shown in Fig. 7a. However, no correlation can be made between the helium implantation profile (Fig. 1) and the distribution of Frank loops through the irradiation depth. A small decrease of mean Frank loop size is quantified with He, however the distribution size for both conditions is very similar as shown on Fig. 7b. Frank loops sizes range from 5 to 70 nm as shown in Fig. 7.

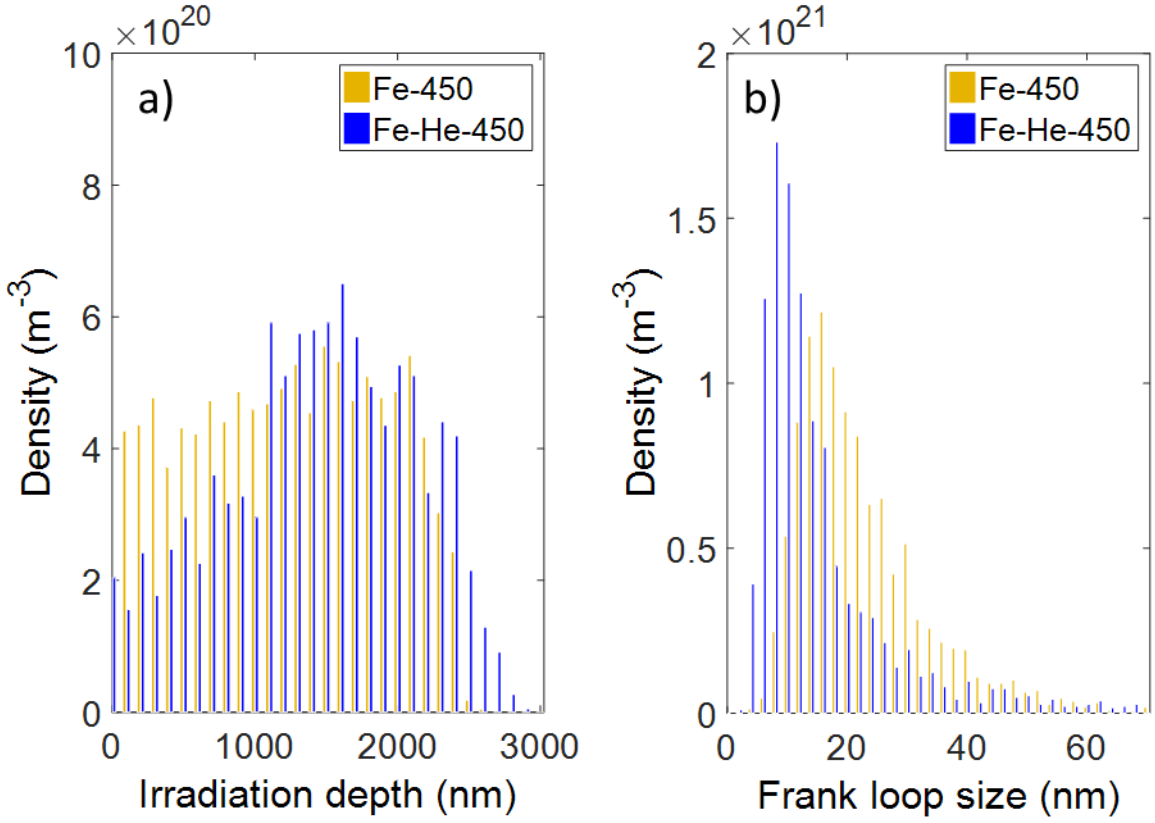

Fig. 7 : Frank loops depth (a) and size (b) distributions in Fe-450 and Fe-He-450 irradiated samples.

B. Hardness measurement

The increase in hardness of the ion irradiated austenitic SS was evaluated by nanoindentation measurements performed at room temperature. Using the data points obtained from nanoindentation measurements, Nix–Gao graphs (i.e. square of nanoindentation hardness plotted as a function of inverse of indent penetration depth) were plotted to avoid the indentation size effect [42] and are shown on Fig. 8 for different irradiation conditions. The hardness data at indentation depth lower than 200 nm are ignored due to reverse indentation size effect and testing artefacts. Results at 600°C and at 450°C are plotted on Fig. 8a and Fig. 8b, respectively. For clarity of the graphs, measurements obtained from the unirradiated area of Fe-600 samples have been reported for both graphs (referred to as "unirradiated"). For unirradiated material, the data show a classical linear evolution where the measured hardness decreases with increase in irradiation depth [35,43,44]. The extrapolated value obtained using linear fitting gave a bulk hardness value H0, of 2 ± 0.2 GPa for all unirradiated samples which is in good agreement with the value obtained in [35] on the same material. It was shown in this study that the Vickers hardness value calculated from Nix – Gao graph was in good agreement with the corresponding Vickers hardness (Hv) measurement (200 ± 30 Hv).

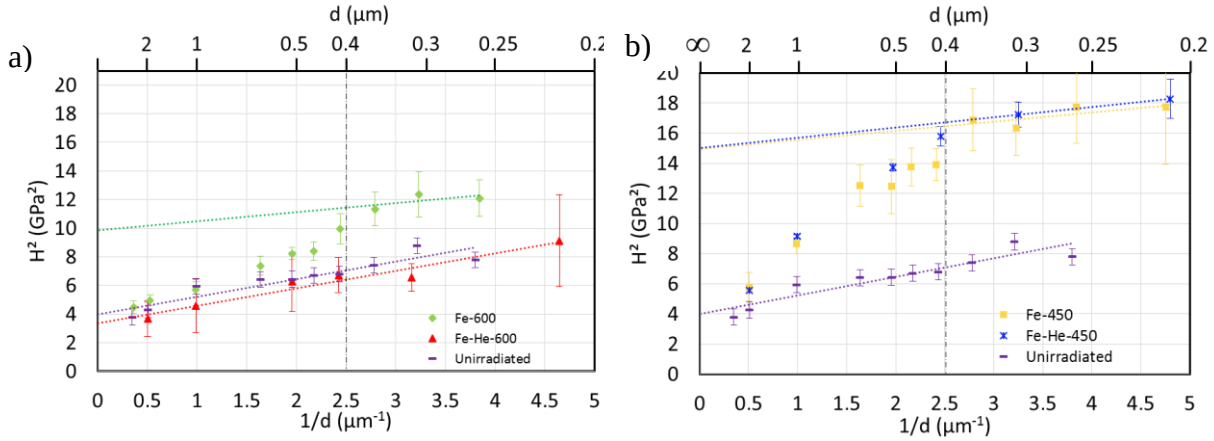

Fig. 8 : Nix-Gao profiles (H^2 versus 1/d) for nanoindentation tests performed on irradiated and unirradiated samples. a) unirradiated, Fe-600 and Fe-He-600 irradiated samples, b) unirradiated, Fe-450 and Fe-He-450 irradiated samples. The unirradiated plot on both figures corresponds to measurements obtained from the unirradiated surface of Fe-600. The hardening ΔH reported in Table 3 is calculated with hardness data of each irradiation condition.

In Fig. 8a) and b), a bi-linearity behavior with an inflexion point is observed for all irradiated samples but Fe-He-600 sample. The depth value corresponding to the inflexion point is slightly different depending on the irradiation conditions: around 0.4 µm for both irradiation at 450°C and around 0.35 µm for Fe-600 irradiations. This inflexion point is strongly related to the depth of the damage layer as it reflects the contribution in hardness from underlying softer substrate which is unirradiated and has been reported in several studies where heavy ions or protons irradiations are used [43,44]. Indents probe a volume that extends deeper than the indentation depth. The probed volume can be 4 to 6 times deeper than the indentation depth [40,45]. It can then be considered in the present study that the volume probed by an indent of depth d extends to ~6 × d. For irradiations at 450°C, although not identical, the trend before the inflexion point is close and for indentation depth larger than 2 µm (1/d=0.5 μm^{-1}) the impact of irradiated layer on hardness becomes negligible and hardness is similar to the one of the unirradiated bulk. For Fe-600 irradiation, it is shown on Fig. 8a that the evolution beyond a depth of 0.35 µm is slightly different to the one observed at 450°C although the irradiated damage depth is similar for both conditions: at 600°C, the hardness measured in the irradiated layer is very close to the hardness of the unirradiated layer for indent depth larger than 1 µm. This discrepancy is thought to result from the markedly different irradiation-induced microstructures between both conditions. The higher void volume fraction in Fe-600 (see Table 2 and Fig. 5i) is inferred to induce a softening contribution in addition to the contribution of the unirradiated region.

The data over the inflection point are interpreted as the hardness of the irradiated region. H0, the hardness at infinite depth is derived from the least square fitting for data between 200 nm and the inflexion point. Fe-He-600 sample shows a significantly different behavior than observed for the other irradiation conditions. As observed for the unirradiated case, a linear behavior is obtained. As discussed in [35], another issue needed to be addressed was the strong variation of the damage profile (Fig. 1) in iron irradiated samples implying a variation of mechanical properties in the irradiated layer. Saturation in density and size of irradiation induced Frank loops has been reported around 5 dpa in ion irradiated austenitic SS [46–48]. The doses considered in this study are all higher than 8 dpa so it was then implicitly assumed that the mechanical properties were constant in the irradiated layer and hence, the hardness value determined could be seen as representative of the irradiated volume.

The hardening values, i.e. the difference between hardness of the unirradiated and irradiated microstructures, for all irradiation conditions are given in Table 3. For each condition, the hardening

was evaluated by considering the unirradiated part of the same sample. Fe-450 irradiation induced the most important hardness increase (78%). Similar hardness increase was observed in Fe-He-450 (77%). Fe-600 shows a much lower hardness (25%) increase than irradiations at 450°C. It is noticeable that hardness on Fe-He-600 samples is close but slightly lower than the unirradiated sample with a bulk hardness value H0, of 1.86 ± 0.31 GPa. It is noted that nanoindentation tests were performed on two different areas of the irradiated part of a Fe-He-600 bar. The hardness profiles measured in the two areas of the irradiated were consistent each other and also the hardness profiles of the unirradiated areas were consistent with those measured for the other irradiations.

Table 3 : Hardening induced by irradiation and metrics to evaluate (crack density, average crack length and crack length per unit area (i.e. total crack length divided by analyzed area)) after SSRT test after 4% plastic deformation for all irradiations

	H (GPa)	ΔH (GPa)	$\%(\Delta H/H_{NI})$	Crack density (cracks/mm^2)	Average crack length (µm)	Crack length per unit area (mm/mm^2)
Fe-600	2.62±0.3	0.52	25	146±20	8.2±2	1.2±0.5
Fe-He-600	1.86±0.3	-0.2	-10	0	0	0
Fe-450	3.9±0.3	1.71	78	347±62	9.7±2	3.4±1.3
Fe-He-450	3.9±0.0	1.70	77	107±21	12±2	1.3±0.5

C. Cracking susceptibility

Irradiated samples were tested under PWR environment to 4% plastic strain at a strain rate of 5.10^{-8} s^{-1} at 340°C and 155 bar. After testing, samples surfaces were observed by SEM to characterize the cracking on the irradiated and the unirradiated zones. SEM observations were made without removing the oxide layer on the tested samples. Very few or no crack were observed for the virgin surface of the samples. On the irradiated surface, depending on the irradiation conditions, cracks existence is observed by using the backscattered electron imaging as shown in Fig. 9. The geometry of cracks suggest that they are intergranular cracks.

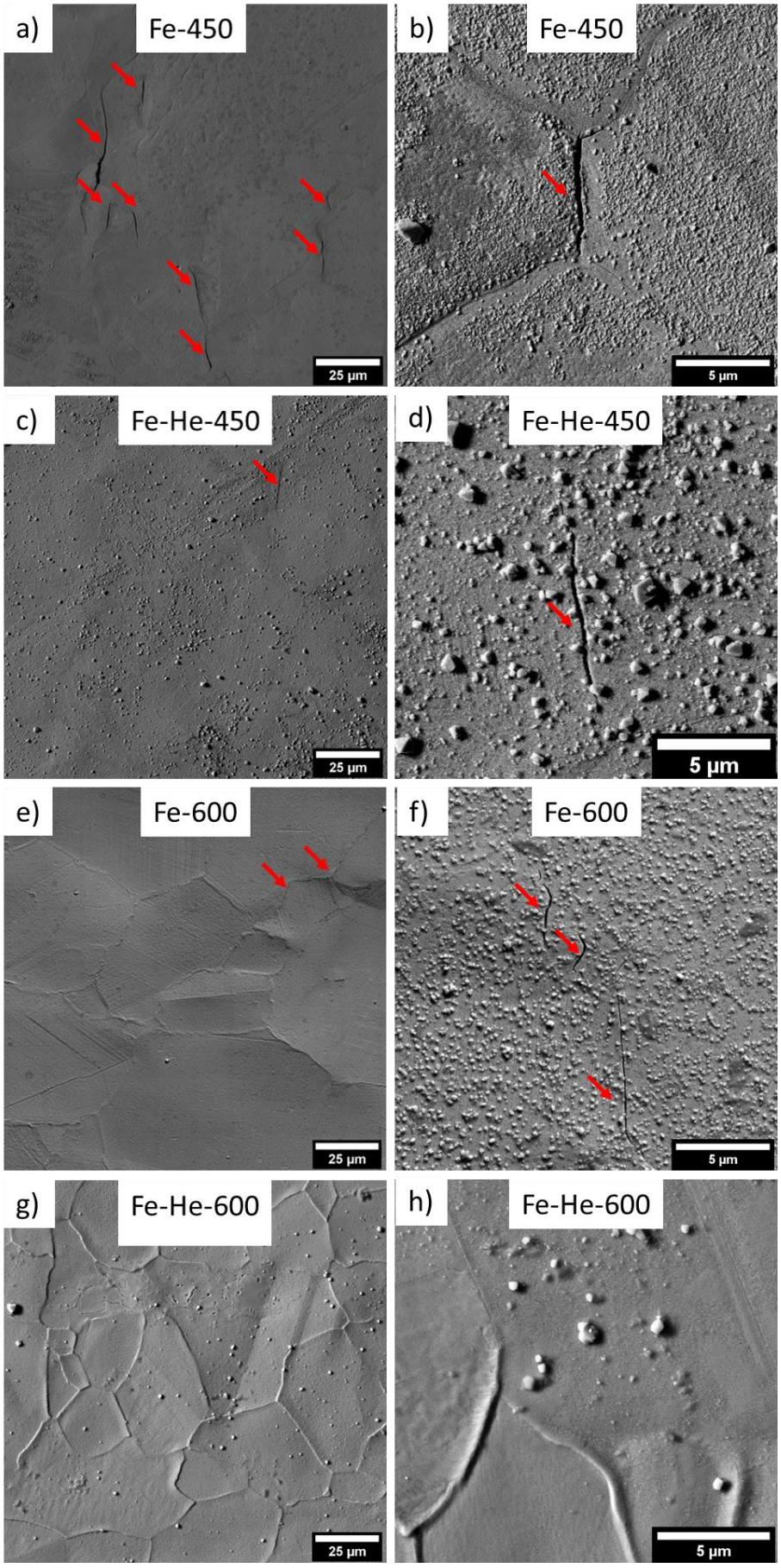

Fig. 9: Surface appearance of SSRT specimens deformed up to 4% plastic strain in PWR environment as observed by SEM in the irradiated area. a) and b) Fe-450, c) and d) Fe-He-450, e) and f) Fe-600, g) and h) Fe-He-600. Cracks are indicated by red arrows. Loading direction is horizontal.

Crack density, average crack length and crack length per unit area, used as metrics to evaluate the cracking susceptibility, on irradiated surfaces are summarizes in Table 3. Fe-450 induced the largest crack density with 347±62 cracks/mm^2. Fe-600 and Fe-He-450[2] still show a significant number of cracks, 146±20 and 107±21 cracks/mm^2, respectively but approximately one third of the crack density obtained for Fe-450. Noticeably no cracking was observed for Fe-He-600 samples after testing under 4% plastic strain. Generally, the cracks observed for Fe-450 condition were more opened than the cracks for Fe-600 with an average opening value of 210 nm and 110 nm, respectively. Whereas the crack density was significantly different between each irradiation conditions, the average crack length is roughly identical for the materials showing cracks with a mean value between 8.2 and 12 µm (see Table 3). Crack length per unit area values confirm the highest cracking susceptibility for Fe-450 condition whereas a similar value is obtained for Fe-He-450 and for Fe-600 (1.2 and 1.3 (mm/mm^2)). Previous study [35] performed on the same SS grade irradiated to 7 dpa with Fe ions at 450°C showed slightly lower crack density (293±18 cracks/mm²) but a higher mean crack length (16±2 µm). Mean cracks orientation is closely perpendicular to the stress axis. Standard deviation from that axis is about 22 degrees.

Several cases of presence of trace of slip lines have been observed on the irradiated surfaces but these traces were not quantified in the present study. It is noted that due to the oxide thickness which can be heterogeneous along the surface, conclusion on the presence of these traces of slip lines is sometimes very difficult. These traces can be inferred on the images reported on Fig. 9e) for Fe-600 conditions. They have also been observed for other conditions but with a lesser extent for Fe-He-600. It is also noted that for several grains showing cracks, presence of trace of slip lines cannot be evidenced. From these qualitative observations, no evident relationship between cracking and intersection of slip lines with grain boundary can be derived in this study.

Based on the parameters considered in the present study to assess intergranular cracking susceptibility (crack presence, crack density, average crack length and crack length per unit area), Fe-He-600 irradiation does not lead to cracking whereas cracking is observed for the other 3 irradiation conditions. Largest effect is induced by the Fe-450 condition as both the crack density and the crack length per unit area are the highest among other conditions.

V. Discussion

This study aims to investigate the link between hardening, susceptibility to IG cracking in PWR environment and the irradiation-induced microstructures. Four different irradiation conditions have been investigated. Our first objective was to obtain void populations with density and size distributions significantly different. Moreover, combining voids with limited irradiation damage was of interest to separate the effect of voids.

[2] It is noted that a BCC phase that covers more than 20% of the sample surface on the irradiated zone of Fe-He-450 sample was revealed from EBSD cartography before straining to 4% in primary water. EDX cartography revealed that chemical composition in this phase is identical to the one of the austenite implying that it is probably martensite. EBSD analysis (not shown here) performed before irradiation on few samples that have undergone the same surface preparation (see section III-A) have not evidenced similar enhancement of martensite formation. Although the underlying mechanism is not understood, it is suspected that martensite was formed under irradiation for Fe-He-450. Such surface fraction of BCC phase was not observed for the other irradiation conditions. Results for Fe-He-450 irradiation are reported here even though the potential impact of martensite beside austenite on cracking susceptibility has not been investigated in this study.

A. *Influence of irradiation conditions on microstructure*

Fig. 4 confirms that irradiation conditions has an impact on void population. Densities and Frank loops size obtained in this study are plotted in Fig. 10 and compared to other studies on heavy-ion (Fe or Ni) irradiated SS at temperature between 400°C and 500°C. Values for density and size are in good agreement to the densities obtained in other studies [35,49–54] but at 8 dpa where our values are a bit higher.

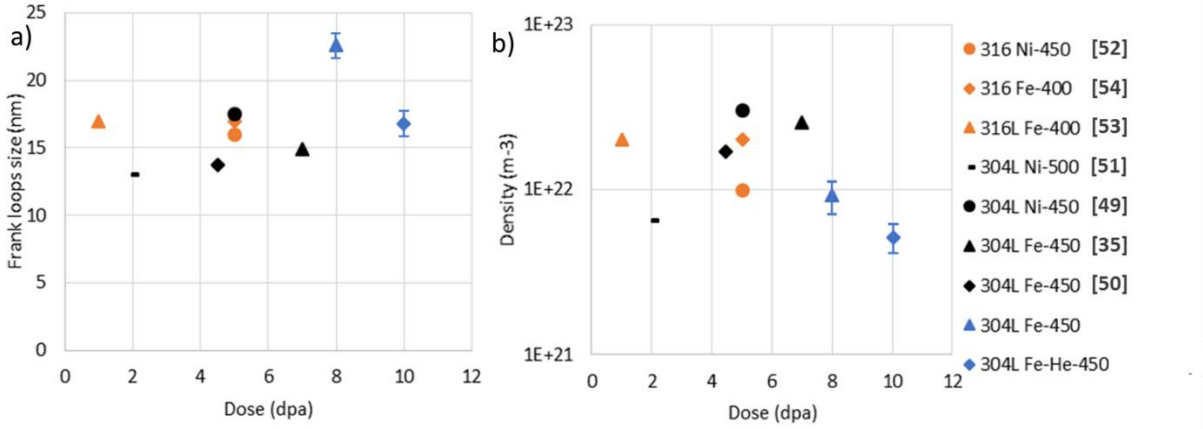

Fig. 10 : Comparison of the Frank loops mean size (a) and density (b) observed in iron irradiated samples (in blue closed symbols) used in this study with ion literature (black symbol for 304L and orange symbol for 316) [35,49–54]. Type of ions and temperature are reported besides the references. Data of our study have been averaged over the first 200 nm of the irradiated layer. Data from literature are reported at the surface. The error bars in b) represents the uncertainty in the estimation of number density of the Frank loops observed including the uncertainty in the foil thickness.

Frank loops density at 450°C ($1.1x10^{22}$ m^{-3}) obtained in this study is in good agreement with the density reported in [55] ($1.9x10^{22}$ m^{-3}) after using Ni^{2+} ions for irradiation at 500°C and 15 dpa, but the size is higher (22.4nm vs 12.5 nm). Regarding comparison with neutron irradiation, Frank loops density and size obtained in our study shows a good agreement with results reported in [56,57] for austenitic stainless irradiated at 375 to 400°C. Higher density (~2-15 10^{22} m^{-3}) and smaller loop size (~10 nm) are generally reported in neutron irradiated stainless steels at temperature ranging between 275°C [58] and 330°C-340°C (see e.g. [59]). Similar trend to have larger loop size and lower density using self-ions than neutron-irradiated was also reported in [55]. As higher density number and smaller loop size are expected at lower temperature, it would be feasible to obtain a closer match with neutron-irradiated 304L by fine-tuning the irradiation temperature. The very low density of Frank loops observed at 600°C in our study is in agreement with the results reported in [55] at the same temperature after 5 MeV Fe^{2+} and 15 dpa on a 304L grade.

Effect of the He/dpa ratio on the Frank loop population was reported in [60]. Higher He/dpa ratio leads to higher density and smaller size. In our study, He co-implantation at 450°C leads also to smaller Frank loop size but the density was not modified. For voids features, comparison with other studies is less stringent as cavities features are related to the material composition (major and minor elements), the damage rate which may differ between studies, but also depends strongly to the irradiation mode as described in [61] and [62].

B. *Impact of the microstructure on hardening*

Irradiations impacts the hardness of a material because of defects like dislocation loops or voids that act like barriers for moving dislocation thus increasing the hardness. Nanoindentation tests shows that the hardness of the irradiated material changes from unirradiated state for every irradiation condition. However, in the case of Fe-He-600 softening is observed. For Fe-He-600, an average voids volume

fraction of ~8.7% has been evaluated based on the whole depth of the irradiation layer. As damage gradient varies more than five times from the surface to the peak, it is important to understand the adequate contribution to hardness measured and reported on Fig. 8. Based on TEM observations of the microstructure, Fig. 5(i) shows that void volume fraction varies from less from 1% at the surface up to 25% at the damage peak with values higher than 2.5% at 300 nm with a strong increase of the volume fraction after 700 nm (> 10%). It is recalled here that using nanoindentation technique, indents probe a volume that extends deeper than the indentation depth so that the first hardness value reported on Fig. 8 for Fe-He-600 (~200 nm) correspond to a scanned zone of about ~1200 nm (~6*d where d is the depth of the indent), i.e. with the contribution of areas where the void volume fraction is higher than 10%. This high level of swelling leads to a decrease of yield strength. This effect can be seen in austenitic SS with long neutron exposure that exhibit large swelling levels [63–65].

When swelling is relatively low, the microstructure can be linked to hardening considering the dispersed barrier model. Equation (1) translates this effect by considering the evolution of yield stress of a kind of defect k $\Delta\sigma_{Y,k}$:

$$\Delta\sigma_{Y,k} = M\mu b\alpha_k(N_k d_k)^{1/2} \quad (1)$$

α is the strength factor of the defect considered, N the defect density, d the defect size, M the Taylor factor of the material (3.06 for austenitic SS), μ is the shear modulus and b is the burgers vector modulus. This model is representative of the Orowan hardening model. Usually when several point obstacles are considered in the microstructure, a superposition law has to be considered, either as a sum of square-root or as linear sum, depending on the relative obstacle strengths. Square root is generally considered in the literature for defects with different hardening strength factor as Frank loops and voids (see e.g. [18]). Linear superposition is generally used for defects with close hardening factor (see e.g. [66]). Considering the presence of voids with strength factors taken to 0.2 (small He-filled voids) and 1 (large voids) and Frank loops, a square root superposition was assumed in the present study as in [18] where Frank loops and voids were also considered:

$$\Delta\sigma_Y = \left[\sum(\Delta\sigma_{Y,k})^2\right]^{1/2} \quad (2)$$

Defects considered for the calculations are the Frank loops and voids observed by TEM. Strength factor considered for Frank loops are reported between 0.3 and 0.5 in the different studies [17,18,21]. A value of 0.5 is chosen in this study. Strength factor considered for voids and small helium filled cavities are taken from [17], i.e. 1 for voids and 0.2 for helium filled cavities. For comparison, the hardening is also calculated for Fe-He-600. Small voids with mean size 8.7 nm are ~~then~~ considered helium-filled cavities. Thus, the strength factor considered is 0.2.

For comparison with hardening measured by nanoindentation a conversion between Berkovich hardness and yield stress is needed. Considering conversion between Vickers and Berkovich hardness and conversion between yield stress and Vickers hardness in equation (3).

$$HV = 94.5\ H\ (2) \text{ and } \Delta\sigma_Y = 3.03\ \Delta HV \quad (3)$$

One can obtain the conversion between Berkovich hardness and yield stress in equation (4).

$$\Delta\sigma_Y = 289.17\ \Delta H \quad (4)$$

Comparison between calculated hardening and hardening derived from the nanoindentation measurements is given on Fig. 11.

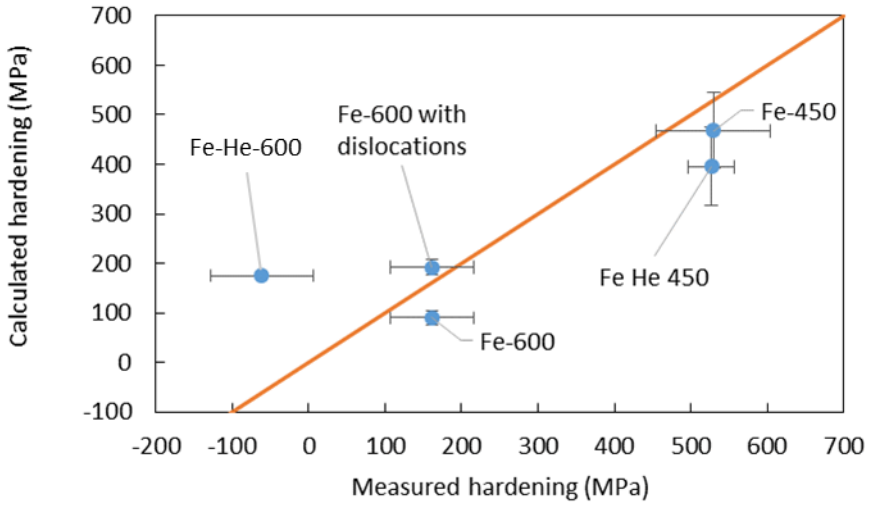

Fig. 11: Comparison between measured hardening and calculated hardening based on equations (1)-(4). The error bars in the figure represents the uncertainty in the estimation of number density and mean size of the defects observed (Table 2).

It is observed on this figure, that considering the different approximations made in equations 2 to 4, a quite good agreement is obtained at 450°C and for Fe-600, although measured hardenings show a trend to slightly underestimate the calculated one. It is noted that an improvement is obtained for Fe-600 when considering the dislocation density increase that has been reported after irradiation at 600°C on the same material [67]. A larger discrepancy is however observed for the Fe-He-600 condition. As for Fe-600, Frank loops density is considered very low for this condition and voids are inferred to be at the origin of the hardening contribution. Considering the voids density and mean size reported in Table 2, voids should lead to a positive hardening of the order of the one observed for Fe-600. However, no hardening and even a slight softening was obtained from the nanoindentation tests. As mentioned earlier, it is inferred that the measured hardness results from the (positive) contribution of voids to hardening and from the (negative) contribution of a high void volume fraction that will led to a softening behavior. Based on these results, when voids volume fraction is limited, it is concluded that the measured hardening results from the contribution of voids and Frank loop. At 450°C, Frank loops contribute mainly to the hardening.

C. Impact of microstructure hardening on cracking susceptibility

Link between hardening and cracking susceptibility is investigated in

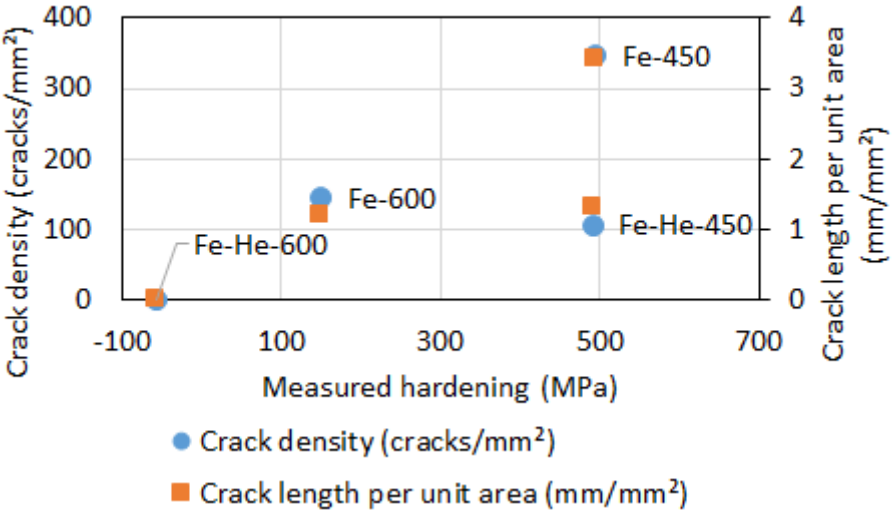

Fig. 12. Both crack density and crack length per unit area are reported as a function of the measured hardening on this figure. It is shown in Table 3 that crack density and crack length per unit area lead to a similar cracking susceptibility behavior between the four irradiation conditions so that only crack density will be considered in the following.

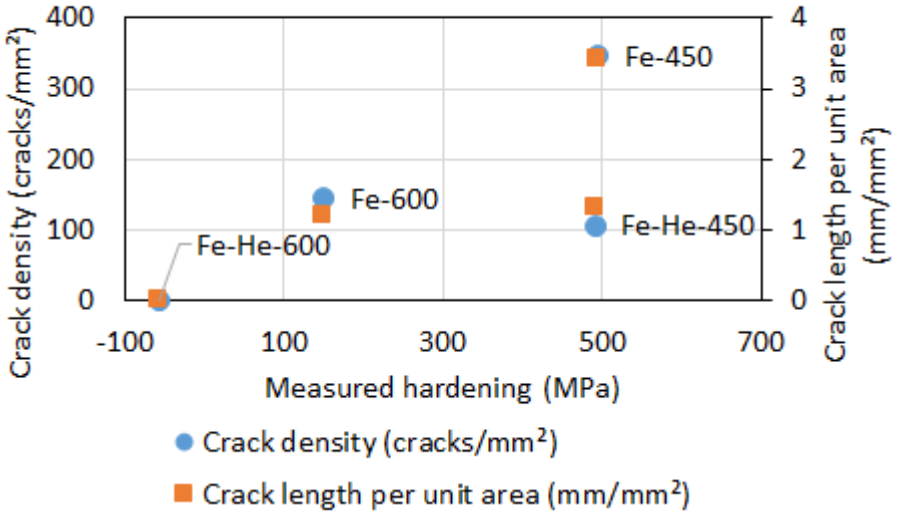

Fig. 12: Mean crack density and total crack length per unit area as a function of measured hardening (Table 3) observed for the different irradiation conditions.

Regarding Fe-He-600, Fe-600 and Fe-450, a good correlation is observed between cracking susceptibility and hardening: cracking susceptibility increases with increasing hardness. This correlation has been reported in several studies and such trend has been also reported recently on Ni-base alloys tested in NWC (Normal Oxygenated Water Chemistry) or PW (Pressurized Water) [14]. Highest cracking susceptibility is observed for Fe-450, which also shows the highest hardening. At the other end, Fe-He-600 with a non-hardening (softening) behavior does not show any cracking susceptibility. Fe-600 with a moderate hardening has an intermediate cracking susceptibility. However, Fe-He-450 behavior with a similar hardening than Fe-450 shows a moderate cracking sensitivity similar to the one observed for Fe-600.

A first attempt of interpretation of the results reported on Fig. 12 could be done by considering two of the contributors to intergranular cracking susceptibility reported in the literature: hardening and enhanced localization of deformation. A difference of behavior has been reported between neutron/proton and heavy ion irradiation regarding enhancement of localization of deformation. Higher localization of deformation (as measured by average slip lines height or average distance between traces of slip line at surface) is observed after neutron/proton than after heavy ion irradiation (see e.g. [35]. This difference is attributed by Jiao and al. [68] to the different penetration depths (more precisely to damage depth relative to the grain size) of protons and heavy ions in the material. Although less marked than for proton, increase of localized deformation (measured by average distance between traces of slip line at surface) has been reported after heavy ion irradiation at 3 and 7 dpa after 5 MeV Fe [34,35] and for 200 keV He and 2.8 MeV Fe in Ref. [48] so it appears of interest to identify any potential difference between the four irradiated microstructures regarding localized deformation.

Formation of defects reduced channel bands, which leads to enhanced localization of deformation, are linked to the presence of defects as Frank loops [69–71]. Considering the very weak density of Frank loops observed after 600°C irradiations (for both Fe-600 and Fe-He-600, see Table 2), enhanced localization is limited after irradiation at 600°C so that the cracking susceptibility, observed for Fe-600 is not expected to be a direct consequence of localized deformation increase. For 450°C irradiation, Frank loop defects were found with a significant density (see Table 2 and it was reported in previous studies on the same 304L material [34,35] an increase, even if rather low, of localized deformation after irradiation at 450°C. Similar cracking behavior of Fe-600 and Fe-He-450 would then lead to the conclusion that a certain amount of hardening in the studied irradiated materials can conduct to a moderate cracking susceptibility.

Different cracking behavior of Fe-450 and Fe-He-450 although they have a similar (high) hardening questions on a potential different behavior regarding strain localization in these two materials. Density of Frank loops, which has been shown to be linked to localization, i.e. increasing localization with increasing density [18], is similar for both materials with a mean density of ~1.1×10^{22} m^{-3}. Regarding irradiation induced microstructure, the main difference between these two materials is the voids population (see Fig. 4 and Table 2) so that a potential effect of these voids on localized deformation is discussed in the following. A link between voids density and size and localization was reported in [18] where it is observed that localization of deformation tends to decrease with higher voids density and size. Based on this observation, it can be inferred that Fe-He-450, which has a two-order magnitude higher density of voids than Fe-450 (see Table 2), has a limited localization of deformation compared to Fe-450. Based on this assumption, higher susceptibility of Fe-450 to cracking susceptibility would result from a higher level of localization whereas localization would be limited due to high density of small voids in Fe-He-450. Further understanding is however needed based on investigation of localization either from TEM studies or from AFM measurements at the grain surface after deformation for these two materials. Besides a different behavior regarding localization of deformation which needs to be further investigated, a potential origin of the different cracking susceptibility between Fe-450 and Fe-He-450 could be the presence of a BCC phase observed for Fe-He-450 material (see section IV-C) with a surface fraction of about 20% in the irradiated area. Based on EBSD cartography and EDX analysis, this phase is inferred to be martensite. Role of martensite in cracking susceptibility would have to be further studied, however, if any, the results of this study show a decrease cracking susceptibility with higher amount of this phase.

A last point related to the objectives of this study is the effect of He implantation on the irradiation-induced microstructure and its potential effect on intergranular cracking susceptibility. The discussion

is focused on the results obtained at 450°C as the irradiation-induced microstructure (Frank loops and voids) is more representative of the microstructure of PWR neutron irradiated 304L components. He has been co-implanted in Fe-He-450 material with an average level of 10-15 appm/dpa which corresponds to those encountered in PWRs. This co-implantation leads to a strong modification of voids population with a decrease of mean voids size (from 21.7 to 8 nm) and a marked increase of density (~x60). The voids volume fraction obtained (0.2%) is in agreement with the upper bound reported in neutron irradiated materials in PWR conditions (see e.g. [72,73]). Another marked effect of He implantation is the presence of intergranular nanocavities which are smaller than their counterparts in the alloy matrix (similar effect being observed at 600°C). As reported in the introduction section the role of these cavities on intergranular fracture and on IASCC susceptibility is still questioned [24,25]. Based on the heavy ions performed in this study, comparison of Fe-450 and Fe-He-450 cracking susceptibility shows that He implantation with level of 10-15 appm/dpa does not increase the susceptibility to intergranular cracking in PWR environment. This result can be firstly interpreted based on the spacing between intergranular cavities (~55nm) and He concentration (<1at.%). These values are respectively higher and smaller than the conditions leading to grain boundary embrittlement reported in [23]. It is then concluded that the irradiation conditions used in our study appear to be not sufficient to increase the cracking susceptibility despite the high hardening of the matrix.

VI. Conclusion

10 MeV Fe^{5+} ion irradiations at 450°C and 600°C up to a surface damage of ~10 dpa and with or without He implantation were conducted on 304L SS samples to obtain different microstructures regarding voids and Frank loop populations. Impact of these microstructures on mechanical properties and intergranular cracking susceptibility in PWR's environment was studied. The following results have been achieved:

- Void populations have been obtained for all the irradiations conditions whereas Frank loops were observed only at 450°C. 600°C irradiations lead to a marked increase of the voids size. Average void volume fraction over the irradiation layer ranges between 0.2 and 0.3% at 450°C whereas it reaches 2.7% and 8.7% at 600°C. Significant variation of the voids volume fraction is observed along the depth of the irradiation layer due to the marked damage gradient inherent to heavy ion irradiation performed in this study.
- Helium implantation leads to a decrease of the mean cavity size with the formation of a population of small cavities (~8nm) with a high density. Small intergranular cavities were observed only for He implanted materials. Frank loops density is unaffected by helium whereas it leads to a decrease of the mean size.
- The highest hardening was obtained at 450°C which is similar with and without He implantation. Moderate hardening was quantified for the irradiation at 600°C without He while irradiation at 600°C with He shows no hardening (indeed a slight softening) behavior inferred to be linked to the high void volume fraction for this irradiation condition.
- Intergranular cracking susceptibility was induced after irradiation for all conditions but Fe-He-600.
- Good correlation between hardness increase and intergranular cracking susceptibility was observed for all conditions, but Fe-He-450 which shows a moderate cracking susceptibility and a high hardening. Microstructure Fe-He-600 with no hardening does not show cracking susceptibility.

- He implantation performed in this study does not increase the susceptibility to intergranular cracking despite the presence of intergranular voids which are smaller than their counterparts in the alloy matrix.
- Interpretation of the difference of cracking behavior between materials with and without He implantation at 450°C is proposed through the limitation of enhanced localization of deformation which would be induced by the large density of intragranular small voids induced by He implantation. Further understanding will be gain based on investigation of deformation localization either from TEM studies or from AFM measurements at the grain surface after deformation. For Fe-He-450, potential impact of martensite beside austenite on cracking susceptibility has not been investigated in this study.

VII. Acknowledgement

This project has received funding from the Euratom research and training program 2014-2018 under Grant Agreement No 661913. This work reflects only the authors' view and the Commission is not responsible for any use that may be made of the information it contains. The authors would like to thank JANNuS platform (DMN/JANNUS, CEA Saclay) for their support and assistance in conducting simple and dual-beam irradiations. FIB machining at CEA Saclay DEN/DANS/DMN was allowed by the project “Investissement d’avenir” GENESIS.

VIII. References

[1] S.J. Zinkle, G.S. Was, Materials challenges in nuclear energy, Acta Materialia. 61 (2013) 735–758. doi:10.1016/j.actamat.2012.11.004.

[2] V. Barabash, A. Peacock, S. Fabritsiev, G. Kalinin, S. Zinkle, A. Rowcliffe, J.-W. Rensman, A.A. Tavassoli, P. Marmy, P.J. Karditsas, F. Gillemot, M. Akiba, Materials challenges for ITER – Current status and future activities, Journal of Nuclear Materials. 367–370 (2007) 21–32. doi:10.1016/j.jnucmat.2007.03.017.

[3] K. Fukuya, H. Nishioka, K. Fujii, M. Kamaya, T. Miura, T. Torimaru, Fracture behavior of austenitic stainless steels irradiated in PWR, Journal of Nuclear Materials. 378 (2008) 211–219. doi:10.1016/j.jnucmat.2008.06.028.

[4] E.A. Kenik, J.T. Busby, Radiation-induced degradation of stainless steel light water reactor internals, Materials Science and Engineering: R: Reports. 73 (2012) 67–83. doi:10.1016/j.mser.2012.05.002.

[5] O.K. Chopra, A.S. Rao, A review of irradiation effects on LWR core internal materials – Neutron embrittlement, Journal of Nuclear Materials. 412 (2011) 195–208. doi:10.1016/j.jnucmat.2011.02.059.

[6] O.K. Chopra, A.S. Rao, A review of irradiation effects on LWR core internal materials – IASCC susceptibility and crack growth rates of austenitic stainless steels, Journal of Nuclear Materials. 409 (2011) 235–256. doi:10.1016/j.jnucmat.2010.12.001.

[7] S.M. Bruemmer, E.P. Simonen, P.M. Scott, P.L. Andresen, G.S. Was, J.L. Nelson, Radiation-induced material changes and susceptibility to intergranular failure of light-water-reactor core internals, Journal of Nuclear Materials. 274 (1999) 299–314. doi:10.1016/S0022-3115(99)00075-6.

[8] J. Connerman, Irradiation effects in a highly irradiated cold worked stainless steel removed from a commercial PWR, in: Proceedings of the 12th International Conference on Environmental Degradation of Materials in Nuclear Power System – Water Reactors, 2005.

[9] R.W. Bosch, M. Vankeerberghen, R. Gérard, F. Somville, Crack initiation testing of thimble tube material under PWR conditions to determine a stress threshold for IASCC, Journal of Nuclear Materials. 461 (2015) 112–121. doi:10.1016/j.jnucmat.2015.02.038.
[10] G.S. Was, S.M. Bruemmer, Effects of irradiation on intergranular stress corrosion cracking, Journal of Nuclear Materials. 216 (1994) 326–347. doi:10.1016/0022-3115(94)90019-1.
[11] T. Shoji, S. Suzuki, K.S. Raja, Current status and future of IASCC research, Journal of Nuclear Materials. 258–263, Part 1 (1998) 241–251. doi:10.1016/S0022-3115(98)00304-3.
[12] K. Fukuya, M. Nakano, K. Fujii, T. Torimaru, Y. Kitsunai, Separation of Microstructural and Microchemical Effects in Irradiation Assisted Stress Corrosion Cracking using Post-irradiation Annealing, Journal of Nuclear Science and Technology. 41 (2004) 1218–1227. doi:10.1080/18811248.2004.9726351.
[13] D. Féron, E. Herms, B. Tanguy, Behavior of stainless steels in pressurized water reactor primary circuits, Journal of Nuclear Materials. 427 (2012) 364–377. doi:10.1016/j.jnucmat.2012.03.034.
[14] M. Wang, M. Song, C.R. Lear, G.S. Was, Irradiation assisted stress corrosion cracking of commercial and advanced alloys for light water reactor core internals, Journal of Nuclear Materials. 515 (2019) 52–70. doi:10.1016/j.jnucmat.2018.12.015.
[15] J. Hure, S. El Shawish, L. Cizelj, B. Tanguy, Intergranular stress distributions in polycrystalline aggregates of irradiated stainless steel, Journal of Nuclear Materials. 476 (2016) 231–242. doi:10.1016/j.jnucmat.2016.04.017.
[16] M. Saleh, Z. Zaidi, M. Ionescu, C. Hurt, K. Short, J. Daniels, P. Munroe, L. Edwards, D. Bhattacharyya, Relationship between damage and hardness profiles in ion irradiated SS316 using nanoindentation – Experiments and modelling, International Journal of Plasticity. 86 (2016) 151–169. doi:10.1016/j.ijplas.2016.08.006.
[17] G.E. Lucas, The evolution of mechanical property change in irradiated austenitic stainless steels, Journal of Nuclear Materials. 206 (1993) 287–305. doi:10.1016/0022-3115(93)90129-M.
[18] Z. Jiao, G.S. Was, The role of irradiated microstructure in the localized deformation of austenitic stainless steels, Journal of Nuclear Materials. 407 (2010) 34–43. doi:10.1016/j.jnucmat.2010.07.006.
[19] R. Nakai, K. Yabuuchi, S. Nogami, A. Hasegawa, The effect of voids on the hardening of body-centered cubic Fe, Journal of Nuclear Materials. 471 (2016) 233–238. doi:10.1016/j.jnucmat.2015.09.048.
[20] I. Villacampa, J.C. Chen, P. Spätig, H.P. Seifert, F. Duval, Helium bubble evolution and hardening in 316L by post-implantation annealing, Journal of Nuclear Materials. 500 (2018) 389–402. doi:10.1016/j.jnucmat.2018.01.017.
[21] L. Tan, J.T. Busby, Formulating the strength factor α for improved predictability of radiation hardening, Journal of Nuclear Materials. 465 (2015) 724–730. doi:10.1016/j.jnucmat.2015.07.009.
[22] C.D. Judge, N. Gauquelin, L. Walters, M. Wright, J.I. Cole, J. Madden, G.A. Botton, M. Griffiths, Intergranular fracture in irradiated Inconel X-750 containing very high concentrations of helium and hydrogen, Journal of Nuclear Materials. 457 (2015) 165–172. doi:10.1016/j.jnucmat.2014.10.008.
[23] T. Miura, K. Fujii, K. Fukuya, Micro-mechanical investigation for effects of helium on grain boundary fracture of austenitic stainless steel, Journal of Nuclear Materials. 457 (2015) 279–290. doi:10.1016/j.jnucmat.2014.11.062.
[24] D.J. Edwards, F.A. Garner, S.M. Bruemmer, P. Efsing, Nano-cavities observed in a 316SS PWR flux thimble tube irradiated to 33 and 70 dpa, Journal of Nuclear Materials. 384 (2009) 249–255. doi:10.1016/j.jnucmat.2008.11.025.
[25] I. Villacampa, J.C. Chen, P. Spätig, H.P. Seifert, F. Duval, Helium effects on IASCC susceptibility in as-implanted solution annealed, cold-worked and post-implantation annealed 316L steel, Corrosion Engineering, Science and Technology. 52 (2017) 567–577. doi:10.1080/1478422X.2017.1323709.
[26] M.S. Weschler, Dislocation channeling in irradiated and quenched metals, 1972. https://www.osti.gov/biblio/4688046.

[27] E.H. Lee, T.S. Byun, J.D. Hunn, K. Farrell, L.K. Mansur, Origin of hardening and deformation mechanisms in irradiated 316 LN austenitic stainless steel, Journal of Nuclear Materials. 296 (2001) 183–191. doi:10.1016/S0022-3115(01)00566-9.
[28] W. Karlsen, G. Diego, B. Devrient, Localized deformation as a key precursor to initiation of intergranular stress corrosion cracking of austenitic stainless steels employed in nuclear power plants, Journal of Nuclear Materials. 406 (2010) 138–151. doi:10.1016/j.jnucmat.2010.01.029.
[29] Z. Jiao, G.S. Was, Impact of localized deformation on IASCC in austenitic stainless steels, Journal of Nuclear Materials. 408 (2011) 246–256. doi:10.1016/j.jnucmat.2010.10.087.
[30] M.D. McMurtrey, B. Cui, I. Robertson, D. Farkas, G.S. Was, Mechanism of dislocation channel-induced irradiation assisted stress corrosion crack initiation in austenitic stainless steel, Current Opinion in Solid State and Materials Science. 19 (2015) 305–314. doi:10.1016/j.cossms.2015.04.001.
[31] G.R. Odette, G.E. Lucas, Deformation and fracture in irradiated austenitic stainless steels, Journal of Nuclear Materials. 191–194 (1992) 50–57. doi:10.1016/S0022-3115(09)80010-X.
[32] G.S. Was, S. Taller, Z. Jiao, A.M. Monterrosa, D. Woodley, D. Jennings, T. Kubley, F. Naab, O. Toader, E. Uberseder, Resolution of the carbon contamination problem in ion irradiation experiments, Nuclear Instruments and Methods in Physics Research Section B: Beam Interactions with Materials and Atoms. 412 (2017) 58–65. doi:10.1016/j.nimb.2017.08.039.
[33] R.E. Stoller, M.B. Toloczko, G.S. Was, A.G. Certain, S. Dwaraknath, F.A. Garner, On the use of SRIM for computing radiation damage exposure, Nuclear Instruments and Methods in Physics Research Section B: Beam Interactions with Materials and Atoms. 310 (2013) 75–80. doi:10.1016/j.nimb.2013.05.008.
[34] J. Gupta, J. Hure, B. Tanguy, L. Laffont, M.-C. Lafont, E. Andrieu, Evaluation of stress corrosion cracking of irradiated 304L stainless steel in PWR environment using heavy ion irradiation, Journal of Nuclear Materials. 476 (2016) 82–92. doi:10.1016/j.jnucmat.2016.04.003.
[35] J. Gupta, J. Hure, B. Tanguy, L. Laffont, M.-C. Lafont, E. Andrieu, Characterization of ion irradiation effects on the microstructure, hardness, deformation and crack initiation behavior of austenitic stainless steel:Heavy ions vs protons, Journal of Nuclear Materials. 501 (2018) 45–58. doi:10.1016/j.jnucmat.2018.01.013.
[36] G.S. Was, Fundamentals of Radiation Materials Science, Springer, 2017. https://www.springer.com/gp/book/9781493934362.
[37] W.J. Choyke, J.N. Mcgruer, J.R. Townsend, J.A. Spitznagel, N.J. Doyle, F.J. Venskytis, Helium effects in ion-bombarded 304 stainless steel, Journal of Nuclear Materials. 85 (1979) 647–651. doi:10.1016/0022-3115(79)90333-7.
[38] A. Renault, J. Malaplate, C. Pokor, P. Gavoille, TEM and EFTEM characterization of solution annealed 304L stainless steel irradiated in PHENIX, up to 36 dpa and at 390 °C, Journal of Nuclear Materials. 421 (2012) 124–131. doi:10.1016/j.jnucmat.2011.10.049.
[39] D. Kiener, P. Hosemann, S.A. Maloy, A.M. Minor, In situ nanocompression testing of irradiated copper, Nature Materials. 10 (2011) nmat3055. doi:10.1038/nmat3055.
[40] D. Kiener, A.M. Minor, O. Anderoglu, Y. Wang, S.A. Maloy, P. Hosemann, Application of small-scale testing for investigation of ion-beam-irradiated materials, Journal of Materials Research. 27 (2012) 2724–2736. doi:10.1557/jmr.2012.303.
[41] L.E. Murr, G.I. Wong, R.J. Horylev, Measurement of interfacial free energies and associated temperature coefficients in 304 stainless steel, Acta Metallurgica. 21 (1973) 595–604. doi:10.1016/0001-6160(73)90068-0.
[42] W.D. Nix, H. Gao, Indentation size effects in crystalline materials: A law for strain gradient plasticity, Journal of the Mechanics and Physics of Solids. 46 (1998) 411–425. doi:10.1016/S0022-5096(97)00086-0.
[43] H.F. Huang, J.J. Li, D.H. Li, R.D. Liu, G.H. Lei, Q. Huang, L. Yan, TEM, XRD and nanoindentation characterization of Xenon ion irradiation damage in austenitic stainless steels, Journal of Nuclear Materials. 454 (2014) 168–172. doi:10.1016/j.jnucmat.2014.07.033.
[44] K. Yabuuchi, Y. Kuribayashi, S. Nogami, R. Kasada, A. Hasegawa, Evaluation of irradiation hardening of proton irradiated stainless steels by nanoindentation, Journal of Nuclear Materials. 446 (2014) 142–147. doi:10.1016/j.jnucmat.2013.12.009.

[45] C. Xu, L. Zhang, W. Qian, J. Mei, X. Liu, The Studies of Irradiation Hardening of Stainless Steel Reactor Internals under Proton and Xenon Irradiation, Nuclear Engineering and Technology. 48 (2016) 758–764. doi:10.1016/j.net.2016.01.007.
[46] K.J. Stephenson, G.S. Was, Comparison of the microstructure, deformation and crack initiation behavior of austenitic stainless steel irradiated in-reactor or with protons, Journal of Nuclear Materials. 456 (2015) 85–98. doi:10.1016/j.jnucmat.2014.08.021.
[47] A. Etienne, M. Hernández-Mayoral, C. Genevois, B. Radiguet, P. Pareige, Dislocation loop evolution under ion irradiation in austenitic stainless steels, Journal of Nuclear Materials. 400 (2010) 56–63. doi:10.1016/j.jnucmat.2010.02.009.
[48] T. Miura, K. Fujii, K. Fukuya, Y. Ito, Characterization of deformation structure in ion-irradiated stainless steels, Journal of Nuclear Materials. 386–388 (2009) 210–213. doi:10.1016/j.jnucmat.2008.12.093.
[49] J.I. Cole, S.M. Bruemmer, Post-irradiation deformation characteristics of heavy-ion irradiated 304L SS, Journal of Nuclear Materials. 225 (1995) 53–58. doi:10.1016/0022-3115(94)00672-5.
[50] B. Michaut, Caractérisation et modélisation de l'évolution de la microstructure et du gonflement d'aciers austénitiques représentatifs des internes inférieurs de réacteurs à eau pressurisée sous irradiations aux ions, PhD Thesis, Université Paris-Saclay, 2017.
[51] M. Le Millier, Fragilisation des aciers inoxydables austénitiques sous irradiation-évolution de la microstructure et amorçage de l'IASCC en milieu REP, PhD Thesis, Mines ParisTech, 2014.
[52] A. Volgin, Characterization and understanding of ion irradiation effect on the microstructure of austenitic stainless steels, PhD Thesis, Université de Rouen, 2012.
[53] H.-H. Jin, E. Ko, S. Lim, J. Kwon, C. Shin, Effect of irradiation temperature on microstructural changes in self-ion irradiated austenitic stainless steel, Journal of Nuclear Materials. 493 (2017) 239–245. doi:10.1016/j.jnucmat.2017.06.019.
[54] H.-H. Jin, E. Ko, S. Lim, J. Kwon, Effects of helium and hydrogen on radiation-induced microstructural changes in austenitic stainless steel, Nuclear Instruments and Methods in Physics Research Section B: Beam Interactions with Materials and Atoms. 359 (2015) 69–74. doi:10.1016/j.nimb.2015.07.086.
[55] Z. Jiao, J. Michalicka, G.S. Was, Self-ion emulation of high dose neutron irradiated microstructure in stainless steels, Journal of Nuclear Materials. 501 (2018) 312–318. doi:10.1016/j.jnucmat.2018.01.054.
[56] B.N. Singh, S.J. Zinkle, Defect accumulation in pure fcc metals in the transient regime: a review, Journal of Nuclear Materials. 206 (1993) 212–229. doi:10.1016/0022-3115(93)90125-I.
[57] J. Gan, G.S. Was, Microstructure evolution in austenitic Fe–Cr–Ni alloys irradiated with rotons: comparison with neutron-irradiated microstructures, Journal of Nuclear Materials. 297 (2001) 161–175. doi:10.1016/S0022-3115(01)00615-8.
[58] D.J. Edwards, E.P. Simonen, S.M. Bruemmer, Evolution of fine-scale defects in stainless steels neutron-irradiated at 275 °C, Journal of Nuclear Materials. 317 (2003) 13–31. doi:10.1016/S0022-3115(03)00002-3.
[59] A.-É. Renault, C. Pokor, J. Garnier, J. Malaplate, Microstructure and grain boundary chemistry evolution in austenitic steels irradiated in the BOR-60 reactor up to 120 dpa, (2009) 11.
[60] Y. Katoh, Y. Kohno, A. Kohyama, Dual-ion irradiation effects on microstructure of austenitic alloys, Journal of Nuclear Materials. 205 (1993) 354–360. doi:10.1016/0022-3115(93)90100-D.
[61] E. Getto, Z. Jiao, A.M. Monterrosa, K. Sun, G.S. Was, Effect of irradiation mode on the microstructure of self-ion irradiated ferritic-martensitic alloys, Journal of Nuclear Materials. 465 (2015) 116–126. doi:10.1016/j.jnucmat.2015.05.016.
[62] J.G. Gigax, E. Aydogan, T. Chen, D. Chen, L. Shao, Y. Wu, W.Y. Lo, Y. Yang, F.A. Garner, The influence of ion beam rastering on the swelling of self-ion irradiated pure iron at 450 °C, Journal of Nuclear Materials. 465 (2015) 343–348. doi:10.1016/j.jnucmat.2015.05.025.
[63] V.S. Neustroev, F.A. Garner, Very high swelling and embrittlement observed in a Fe–18Cr–10Ni–Ti hexagonal fuel wrapper irradiated in the BOR-60 fast reactor, Journal of Nuclear Materials. 378 (2008) 327–332. doi:10.1016/j.jnucmat.2008.06.036.

[64] V.S. Neustroev, F.A. Garner, Severe embrittlement of neutron irradiated austenitic steels arising from high void swelling, Journal of Nuclear Materials. 386–388 (2009) 157–160. doi:10.1016/j.jnucmat.2008.12.077.
[65] F.A. Garner, M.B. Toloczko, High dose effects in neutron irradiated face-centered cubic metals, Journal of Nuclear Materials. 206 (1993) 230–248. doi:10.1016/0022-3115(93)90126-J.
[66] C. Pokor, Y. Brechet, P. Dubuisson, J.-P. Massoud, X. Averty, Irradiation damage in 304 and 316 stainless steels: experimental investigation and modeling. Part II: Irradiation induced hardening, Journal of Nuclear Materials. 326 (2004) 30–37. doi:10.1016/j.jnucmat.2003.12.008.
[67] P.O. Barrioz, Rupture ductile des matériaux CFC irradiés, PhD Thesis, Université Paris-Saclay, 2019.
[68] Z. Jiao, G. Was, T. Miura, K. Fukuya, Aspects of ion irradiations to study localized deformation in austenitic stainless steels, Journal of Nuclear Materials. 452 (2014) 328–334. doi:10.1016/j.jnucmat.2014.05.058.
[69] N. Hashimoto, S.J. Zinkle, A.F. Rowcliffe, J.P. Robertson, S. Jitsukawa, Deformation mechanisms in 316 stainless steel irradiated at 60°C and 330°C, Journal of Nuclear Materials. 283–287 (2000) 528–534. doi:10.1016/S0022-3115(00)00087-8.
[70] T.S. Byun, N. Hashimoto, Strain localization in irradiated materials, Nuclear Engineering and Technology. 38 (2006) 619–638.
[71] K. Gururaj, C. Robertson, M. Fivel, Channel formation and multiplication in irradiated FCC metals: a 3D dislocation dynamics investigation, Philosophical Magazine. 95 (2015) 1368–1389. doi:10.1080/14786435.2015.1029560.
[72] H.M. Chung, NRC: Assessment of Void Swelling in Austenitic Stainless Steel Core Internals, 2006. https://www.nrc.gov/reading-rm/doc-collections/nuregs/contract/cr6897/ (accessed September 30, 2019).
[73] C. Panait, Microstructural investigations of a baffle to former bolt located on a high level of the internal structures, in: Fontevraud ,8 France, Avignon, 2014.